Coastal Engineering 179 (2023) 104240

Contents lists available at ScienceDirect

Coastal Engineering

journal homepage: www.elsevier.com/locate/coastaleng

Fully nonlinear investigation on energy transfer between long waves and short-wave groups over a reef

Ye Liu [a], Yu Yao [b], Zhiling Liao [a,c,*], Shaowu Li [a,**], Chi Zhang [d], Qingping Zou [c]

[a] State Key Laboratory of Hydraulic Engineering Simulation and Safety, Tianjin University, Tianjin, 300072, China
[b] School of Hydraulic Engineering, Changsha University of Science and Technology, Changsha, Hunan, 410114, China
[c] The Lyell Centre for Earth and Marine Science and Technology, Institute for Infrastructure and Environment, Heriot-Watt University, Edinburgh, EH14 4AS, UK
[d] College of Harbor, Coastal, and Offshore Engineering, Hohai University, Nanjing, Jiangsu, 210098, China

ARTICLE INFO

Keywords:
Long wave
Coral reef
Energy transfer
SWASH
Breakpoint forcing
Radiation stress

ABSTRACT

Long waves are amplified as short-wave groups shoal and break over reefs, therefore, having significant impacts on coastal inundation, structure stability, and sediment transport. This study investigated the cross-reef variation of long-wave energy exchange with short-wave group over a reef using fully nonlinear analysis of simulation results by the non-hydrostatic model SWASH. The objective was to elucidate the mechanisms of long-wave transformation under nonlinear short-wave group forcing over a reef, and to assess the consequences of simplifications in linear and weakly nonlinear analyses in this problem. The energy transfer between short and long waves is the work done by radiation stress on long-wave velocity. Unlike conventional linear and weakly nonlinear analysis, the Stokes transport and long-wave modulation of local water depth are included in the fully nonlinear analysis. It was found that only the long-wave energy flux gradient given by the fully nonlinear analysis was balanced by the work done by wave radiation stress over a shallow reef. The fully nonlinear analysis showed that strict mass conservation has to be used to extract long wave velocity properly. In contrast, in linear and weakly nonlinear analysis, the long-wave velocity is extracted from single-point velocity measurements. The fully nonlinear analysis demonstrated that the generation and growth of incoming breakpoint-forced long waves overcame the dissipation of bound long waves in the surf zone, leading to amplification of incoming long-wave energy flux. This phenomenon occurred even when short waves mainly broke over the horizontal reef flat with large submergence, indicating that long-wave evolution is not locally controlled but dependent on wave spatial evolution history. Outgoing breakpoint-forced long waves were dissipated considerably during de-shoaling over the forereef due to substantial energy transfer to incoming short waves, though both of them are free waves. The consistent phase coupling between outgoing long waves and incoming short-wave groups at all frequencies was found to be the primary driving mechanism for the energy transfer. According to the fully nonlinear analysis, the reef-flat submergence may affect the long wave in a complex fashion, *i.e.*, reducing the submergence may enhance the energy transfer from short waves to long waves or suppress long-wave growth by increasing its frictional dissipation at the same time.

1. Introduction

Long waves at infragravity (0.005–0.05 Hz) and far infragravity (0.001–0.005 Hz) frequencies are significantly amplified as short-wave groups shoal and break over reefs (Masselink et al., 2019; Pomeroy et al., 2012), and become one of the main hydrodynamic drivers over shallow reef flats. Under certain conditions, long waves may account for 50% of the bottom shear stress (Van Dongeren et al., 2013) and 41% of the runup (Beetham et al., 2016), leading to potential impacts on sediment transport (Pomeroy et al., 2015), shoreline inundation (Cheriton et al., 2016; Roeber and Bricker, 2015), and the performance and stability of coastal structures (Liu et al., 2020; Zou and Peng, 2011). In addition, long waves modulated by tides (Melito et al., 2022) may have considerable effects on estuarine dynamics (Melito et al., 2020) and harbor resonance (Gao et al., 2021; Thotagamuwage and Pattiaratchi, 2014). In recent years, although long-wave motions and their dynamics have received lots of attention (*e.g.*, Péquignet et al., 2014; Pomeroy et al., 2012; Van Dongeren et al., 2013; Zheng et al., 2020), there is

* Correspondence to: Heriot-Watt University, Edinburgh, EH14 4AS, UK.
** Corresponding author.
E-mail addresses: z.liao@hw.ac.uk (Z. Liao), lishaowu@tju.edu.cn (S. Li).

https://doi.org/10.1016/j.coastaleng.2022.104240
Received 12 January 2022; Received in revised form 18 September 2022; Accepted 15 October 2022
Available online 21 October 2022

a lack of study on nonlinear energy transfer between long and short waves that controls the generation and dissipation of long waves over reefs.

Long waves can be generated through bound long wave (Longuet-Higgins and Stewart, 1962) and breakpoint-forced long wave mechanisms (Symonds et al., 1982). Bound long wave is the mean water level fluctuation forced by the radiation stress gradient of a short-wave group. Over a sloping bottom, it consists of equilibrium and non-equilibrium components, which are in-phase and in quadrature with the short-wave group, respectively (Liao et al., 2021; Zou, 2011). Superposition of the components presents a phase lag between the bound long wave and the short-wave group, which allows an enhancement of the long wave in decreasing water depth by gaining energy from the short-wave group. Following short-wave breaking, the bound long wave may decay due to the energy transfer back to the short-wave group (Baldock, 2012; De Bakker et al., 2016b) and the breaking in very shallow water after being released (Van Dongeren et al., 2007). Breakpoint-forced long wave is the dynamic setup induced by the radiation-stress gradient of individual short waves of variable heights during breaking. Shoreward breakpoint-forced long wave in phase with the short-wave group and seaward breakpoint-forced long wave in antiphase with the short-wave group are concurrently generated (Contardo et al., 2018). It is recognized that bound and breakpoint-forced long waves dominate over mild and steep slopes, respectively. Battjes et al. (2004) defined the normalized bottom slope as the relative depth change per long-wave length. Baldock (2012) further incorporated the effect of short-wave steepness in the following surf-beat similarity parameter,

$$\xi_{\text{surfbeat}} = \frac{h_x}{\omega_{\text{low}}}\sqrt{\frac{g}{h_s}}\sqrt{\frac{H_{\text{SW},0}}{L_{\text{p},0}}}, \tag{1}$$

where h_x is the bottom slope, ω_{low} is the long-wave angular frequency, g is the gravitation acceleration, h_s is the characteristic water depth, $H_{\text{SW},0}$ and $L_{\text{p},0}$ refer to off-reef short-wave height and length, respectively. As ξ_{surfbeat} increases for a sloping bottom, the surf beat transits gradually from bound long wave driven to breakpoint-forced long wave driven, with its intensity decreasing first and then increasing (Baldock, 2012).

Unlike a plane slope, however, a reef topography consists of a steep forereef slope followed by a horizontal and submerged reef flat. Therefore, it is challenging to apply the concept of surf-beat similarity directly. In addition, variation of reef-flat submergence during tidal cycles and with sea-level rise modulates the long-wave evolution. Firstly, short-wave breaking may occur not only over the forereef at low submergence but also over the reef flat at high submergence (Yao et al., 2013). In both cases, large breakpoint-forced long waves are present shoreward of the reef surf zone, regardless of local bottom slope of breaking (Masselink et al., 2019). This phenomenon is not well understood. Secondly, previous studies on the variation of long waves with reef-flat submergence are inconclusive and sometimes contradictory. For example, Beetham et al. (2016) found that long waves were most prominent at the mid-tide and smaller at low and high tides at Funafuti Atoll, which was confirmed by the numerical simulations of Masselink et al. (2019). Nevertheless, Beetham et al. (2016) also reported that tide did not modulate long waves under energetic wave conditions, as in the experimental results of Buckley et al. (2018). Furthermore, the experiments of Yao et al. (2020) indicated amplified long waves at shallower submergences, whereas the field observation of Pomeroy et al. (2012) demonstrated the opposite. The inconsistency in these results may be caused by the shoreline reflection, reef-flat resonance, and dissipation due to friction. This obscures the dependence of energy transfer between long and short waves on reef submergence, which is one of the major control factors for long-wave evolution.

Variation of long waves along reefs has been the subject of several recent studies. Some high-resolution physical experiments and numerical modelings showed that long waves increased towards the shore during shoaling over the forereef, followed by a rapid reduction immediately after short-wave breaking (*e.g.*, Buckley et al., 2018; Masselink et al., 2019; Liu et al., 2021a; Yao et al., 2016). Buckley et al. (2018) suspected that the reduction was due to the energy transfer to short waves. Based on a linear wave reflection analysis, Liu et al. (2021a) demonstrated a similar size reduction in incoming long waves. However, whether the reduction of incoming long waves is physically validated has not been tested by rigorous fully nonlinear analysis.

Energy transfer between long and short waves can be physically interpreted as the work done by radiation-stress gradient on long-wave velocity (Phillips, 1977; Schäffer, 1993) or as the result of triad interaction described by the bispectrum of surface elevations (Herbers and Burton, 1997). The two interpretations should be inherently consistent under non-breaking conditions (Liao et al., 2022), but the estimate of energy transfer by bispectral analysis may not be accurate in the surf zone because of its irrotational assumption and classical Boussinesq scaling (*i.e.*, nonlinearity = O(dispersive effect^2)). The bispectral analysis of field data for Ningaloo Reef in Western Australia by Pomeroy et al. (2012) indicated negligible energy transfer between long and short waves shoreward of the reef surf zone. Based on XBeach-Surfbeat simulations for the same reef, Van Dongeren et al. (2013) extracted incoming long waves using a linear method and found that the energy transfers from short waves to incoming long waves in the surf zone remained almost the same at high and low tides. Péquignet et al. (2014) applied a weakly nonlinear long-wave energy balance equation (Henderson et al., 2006) to the field data collected at the fringing reef of Ipan, Guam, without separating incoming and outgoing components. Contrary to Van Dongeren et al. (2013), Péquignet et al. (2014) found that the magnitude of energy transfer was modulated by tidal level and was much larger than the magnitude of frictional dissipation in the surf zone. However, the linear reflection analysis and the weakly nonlinear analysis assume small-amplitude waves, which may have influenced the analysis results. Unlike previous studies, we propose to apply the fully nonlinear energy balance equation derived by Phillips (1977) to well-controlled conditions to resolve these conflicting conclusions.

This study aims to evaluate the low-frequency energy modifications through the generation and dissipation of bound and breakpoint-forced long waves over a reef using fully nonlinear analysis of simulation results by the non-hydrostatic model SWASH (Zijlema et al., 2011). Section 2 describes the numerical simulations and the fully nonlinear energy balance analysis. The analysis results are presented in Section 3. In Section 4, linear and weakly nonlinear analyses are compared with the fully nonlinear analysis. In Section 5, we discuss (a) the impacts of simplifications in the linear and weakly nonlinear analysis; (b) the energy transfer between long and short waves, especially that from outgoing free long waves to incoming short waves over the forereef; and (c) the influence of reef submergence on the generation and dissipation of long waves. Main conclusions are summarized in Section 6.

2. Methods

2.1. Numerical simulations

Numerical simulations were performed using the multi-layer non-hydrostatic model SWASH (Zijlema et al., 2011). Governing equations in the vertical two-dimensional form are the following.

$$\rho\left(\frac{\partial u}{\partial t} + u\frac{\partial u}{\partial x} + w\frac{\partial u}{\partial z}\right) = -\frac{\partial\left(p_{\text{h}} + p_{\text{nh}}\right)}{\partial x} + \frac{\partial \tau_{xz}}{\partial z} + \frac{\partial \tau_{xx}}{\partial x}, \tag{2}$$

$$\rho\left(\frac{\partial w}{\partial t} + u\frac{\partial w}{\partial x} + w\frac{\partial w}{\partial z}\right) = -\frac{\partial p_{\text{nh}}}{\partial z} + \frac{\partial \tau_{zz}}{\partial z} + \frac{\partial \tau_{zx}}{\partial x}, \tag{3}$$

$$\frac{\partial u}{\partial x} + \frac{\partial w}{\partial z} = 0, \tag{4}$$

where ρ is the water density; t is the time; x and z are the horizontal and vertical coordinates, respectively; $u(x, z, t)$ and $w(x, z, t)$ are the horizontal and vertical velocities, respectively; p_{h} and p_{nh} are the hydrostatic and non-hydrostatic pressures, respectively; τ is the turbulent stress

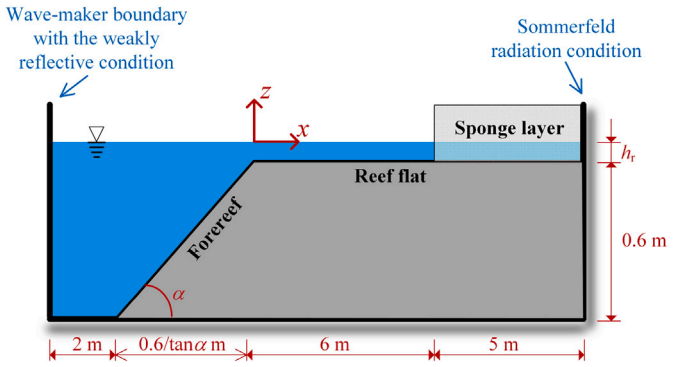

Fig. 1. Illustration of coordinates and set-up for SWASH model simulations of wave group propagating over the idealized reef topography. $x = 0$ is at the intersection of the forereef and the reef flat, and $z = 0$ is at the still water level. $\tan\alpha$ is the slope of the forereef, and h_r is the reef submergence.

Table 1
Model simulation conditions, including the forereef slope ($\tan\alpha$), reef-flat submergence (h_r), and incident significant wave height ($H_{SW,0}$) and spectral peak period (T_p).

Case	$\tan\alpha$	h_r (m)	$H_{SW,0}$ (m)	T_p (s)	$h_r/H_{SW,0}$
A	1/5	0.015	0.06	1.5	0.25
B	1/5	0.045	0.06	1.5	0.75
C	1/5	0.075	0.06	1.5	1.25
D	1/15	0.045	0.06	1.5	0.75

term closed by $k-\varepsilon$ model. The bottom frictional shear-stress term is given by the quadratic friction law with Manning formula,

$$\tau_b = \rho \frac{gn^2}{d^{1/3}} u|u|, \tag{5}$$

where n is the Manning coefficient, and $d = h+\zeta$ is the total water depth with h the still water depth and ζ the free surface elevation relative to the still water level. According to the SWASH manual, the Manning formula provides a good representation of wave dynamics in the surf zone.

The SWASH model has been extensively validated against laboratory and field data for reefs and beaches by the authors (Liu and Li, 2018; Liu et al., 2021a,b) and others (e.g., De Bakker et al., 2016b; Lowe et al., 2015; Rijnsdorp et al., 2015; Risandi et al., 2020; Torres-Freyermuth et al., 2012). An additional validation against the platform-reef data of Masselink et al. (2019) is shown in Appendix A. However, the SWASH model cannot properly reproduce the overturning of plunging breaker in reef environments, since it uses a single value function to track the free surface.

Numerical simulations of irregular waves were performed in a vertically two-dimensional numerical flume (Fig. 1), where a reef of height 0.6 m was located 2 m away from the wave-maker boundary. Four cases with incident significant wave height ($H_{SW,0}$) of 0.06 m and peak period (T_p) of 1.5 s were investigated (Table 1). Cases A–C had the same forereef slope ($\tan\alpha = 1/5$) but different ratios of reef-flat submergence to incident wave height ($h_r/H_{SW,0} = 0.25, 0.75, 1.25$) that control the incipient breaking location and breaking intensity (Yao et al., 2013). Case D with $\tan\alpha = 1/15$ and $h_r/H_{SW,0} = 0.75$ was simulated for comparison with Case B. The forereef slopes were within the range (1/1–1/20) summarized by Quataert et al. (2015). Time series of incident short waves were synthesized from the JONSWAP spectrum with a peak enhancement factor of 3.3, and the same initial phases were used for all cases to minimize the uncertainty of long waves induced by different short-wave sequences (Liu et al., 2021b).

Six equivalent vertical layers and a uniform horizontal grid size of 0.02 m were used following De Bakker et al. (2016b). The duration of each simulation was 30.5 min. Model results of velocity, pressure, and surface elevation were output at the last 30 min with a time interval of 0.1 s.

Following Rijnsdorp et al. (2014), waves at the left boundary were driven by the horizontal velocity of incoming (u_i) and outgoing (u_o) components, where $u_i(z,t)$ was the sum of target linear short waves and nonlinear bound long waves, and $u_o(t) = \sqrt{gd}\left(\zeta - \zeta_t\right)/d$ was the depth-averaged velocity due to difference between the target surface elevation (ζ_t) and the instantaneous surface elevation (ζ) computed by SWASH. The good performance of the adopted boundary condition in suppressing the generation of spurious free long waves and minimizing the re-reflection is demonstrated in Appendix B. A Sommerfeld condition and a sponge layer were prescribed at the outlet boundary to absorb long and short waves, respectively. Compared with the fringing reef with a shoreline (*e.g.*, Péquignet et al., 2014; Yao et al., 2020) and the platform reef with an abrupt topography change at the reef end (*e.g.*, Masselink et al., 2019; Zhu et al., 2021) (see Fig. A.12e–f), changes of long-wave energy due to the reflection at the right boundary and the reef-flat resonance were largely excluded to focus on the energy change induced by nonlinear energy transfer.

Since nonlinear energy transfer is the main focus, a numerical modeling set-up without bottom friction that would simplify the model result analysis is appealing. Nevertheless, bottom friction can be considered to make the analysis more general. Selection of an appropriate Manning coefficient value for wave simulations with multi-layer models is not straightforward, since the Manning formula is derived for quasi-steady flow and is associated with depth-averaged flow velocities while bottom shear stress of oscillatory waves is calculated with near-bottom velocities. Therefore, the Manning coefficient is not necessarily related to the apparent roughness. For example, Melito et al. (2022) found an optimal Manning coefficient $n = 0.045$ s/m$^{1/3}$ for simulating waves over a natural sandy beach with medium-to-fine sand ($d_{50} = 0.14 - 0.3$ mm). In the present study, $n = 0.025$ s/m$^{1/3}$ was adopted. The dissipation due to bottom friction within the surf zone tends to be much smaller than the breaking-induced dissipation, and flow perturbations by bottom friction are most significant close to the seabed (Zou et al., 2006). It was found that the numerical viscosity varying with the temporal and spatial schemes may also have significant impacts on computational results of breaking waves (Wang et al., 2009). Although the calculated equivalent roughness scale was quite high compared with the water depth from the perspective of unidirectional open channel flow, it will be shown in Section 3.4 that the friction dissipation of long waves was small with $n = 0.025$ s/m$^{1/3}$.

2.2. Data analysis

2.2.1. Energy balance

This study calculated the work done by the radiation-stress gradient on the long-wave velocity to evaluate the energy transfer. Neglecting dissipation terms, Ruju et al. (2012) and Mendes et al. (2018) demonstrated the energy balance of bound long waves over mild slopes, except for the inner surf zone where long-wave breaking may occur. The present study investigated group-induced long waves over a typical reef topography where bound and breakpoint-forced long waves coexist. Particularly, incoming and outgoing long waves were examined separately.

The one-dimensional time-averaged fully nonlinear energy balance equation of long wave reads (Phillips, 1977; Schäffer, 1993),

$$\frac{\partial F}{\partial x} = R + D, \tag{6}$$

where F is the long-wave energy flux; R is the energy transfer rate between long and short waves; D denotes the dissipation rate due to bottom friction, and the internal viscous dissipation is assumed negligible. Note, long waves may break in very shallow water close to the shoreline where short waves have almost been dissipated (Van Dongeren et al., 2007). However, considerable short waves left in the surf zone of coral reefs may restrain long-wave breaking, which will be supported by the good balance of Eq. (6) in Section 3.

Assuming a hydrostatic pressure for long waves, the long-wave energy flux is estimated by

$$F = \overline{\overline{U(h+\bar{\zeta})\left(\frac{1}{2}\rho U^2 + \rho g\bar{\zeta}\right)}}, \tag{7}$$

where U is the long-wave velocity defined by depth-averaging the low-frequency mass transport as,

$$U = \frac{1}{h+\bar{\zeta}}\overline{\int_{-h}^{\zeta} u\,\mathrm{d}z} - Q_c. \tag{8}$$

with $Q_c = \overline{\overline{\int_{-h}^{\zeta} u\,\mathrm{d}z}}$ the mean flux. By definition, $\overline{(\bullet)}$ and $\overline{\overline{(\bullet)}}$ denote the time averaging over short- and long- wave periods, respectively. In practice, we used a low-frequency band pass filter with the cut-off frequency of $f_p/2$ ($f_p = 1/T_p$) as $\overline{(\bullet)}$ and the averaging over the entire duration of data as $\overline{\overline{(\bullet)}}$. Eq. (8) differs slightly from those of Mei et al. (2005, Eq. (11.2.1)) and Ruju et al. (2012, Eq. (2)) in that it distinguishes between long wave and mean current by forcing the net mass transport of long wave to be zero.

The energy transfer rate between long and short waves is given by

$$R = -\overline{\overline{U\frac{\partial S}{\partial x}}}, \tag{9}$$

$R > 0$ indicates a nonlinear energy transfer from short to long waves, and $R < 0$ suggests the inverse transfer.

S is the wave radiation stress,

$$S = \overline{\int_{-h}^{\zeta}\left(\rho u'^2 + p\right)\mathrm{d}z} - \frac{1}{2}\rho g(h+\bar{\zeta})^2, \tag{10}$$

with $u' = u - \overline{\int_{-h}^{\zeta} u\,\mathrm{d}z}\Big/\left(h+\bar{\zeta}\right)$ the velocity deviation from the mean (Mei et al., 2005, Eq. (11.2.2)), and $p = p_h + p_{nh}$ the total pressure. The definition of u' was promoted by Ruju et al. (2012) because it avoids the extrapolation of velocities above wave troughs while resulting in the radiation stress equivalent to that proposed by Phillips (1977). Nevertheless, the radiation stress and its gradient from post-processing calculations may deviate slightly from those of the numerical model (da Silva et al., 2021).

The energy dissipation rate due to bottom friction is given by

$$D = -\overline{\overline{U\tau_b}}. \tag{11}$$

2.2.2. Separation of incoming and outgoing long waves

Surface elevations are decomposed as

$$\zeta - \bar{\bar{\zeta}} = \zeta_{SW} + \zeta_{LW}, \tag{12}$$

where ζ_{SW} and ζ_{LW} are surface elevations of short and long waves, respectively. They are separated using a band-pass filter with a cut-off frequency of $f_p/2$. Note that $\bar{\zeta} = \bar{\bar{\zeta}} + \zeta_{LW}$.

Incoming (+) and outgoing (-) long-wave components are separated according to mass conservation (Van Dongeren and Svendsen, 1997),

$$\zeta_{LW}^{\pm} = \frac{c^{\mp}\zeta_{LW} \pm (h+\bar{\zeta})U}{c^+ + c^-}, \tag{13}$$

$$U^{\pm} = \pm\frac{c^{\pm}}{h+\bar{\zeta}}\zeta_{LW}^{\pm}, \tag{14}$$

where c is the phase celerity of long waves. Eq. (14) was initially derived for a spatially non-varying long wave over a horizontal bottom (Van Dongeren and Svendsen, 1997), but was later shown to apply to a sloping bottom by Battjes et al. (2004).

Over the horizontal bottom seaward of the reef, incoming long wave is known as the equilibrium bound long wave propagating at the celerity of short-wave group (c_g). As waves enter the shoaling zone over the forereef, the bound long wave is no longer in equilibrium with the group forcing, as indicated by the ostensible lag between bound long wave and the short-wave group (*e.g.*, Janssen et al., 2003). From this perspective, c^+ seems to be smaller than c_g. However, the theoretical solutions for group-forced long waves (Janssen et al., 2003; Liao et al., 2021; Zou, 2011) reveal that the lag is due to the presence of non-equilibrium bound long wave in quadrature with the short-wave group, and both equilibrium and non-equilibrium bound long waves still propagate at the group celerity. In the surf zone, however, bound and breakpoint-forced long waves may co-exist since breakpoint may not be the release location of bound long wave (Baldock, 2012), making it difficult to determine c^+. In this study, c^+ is tentatively given by the free long-wave celerity. In summary, $c^{\pm}$ are formulated as,

$$c^+ = \begin{cases} c_g & x < x_b \\ \sqrt{g\left(h+\bar{\zeta}\right)} & x \geq x_b \end{cases}, \tag{15}$$

$$c^- = \sqrt{g\left(h+\bar{\zeta}\right)}, \tag{16}$$

where c_g is calculated at the peak frequency, which is a good approximation of the actual celerity of the wave group (Janssen et al., 2003); x_b is the breakpoint location.

By substituting $\zeta_{LW} = \zeta_{LW}^+ + \zeta_{LW}^-$ and $U = U^+ + U^-$ into Eq. (7), the net energy flux is expressed by

$$F = F^+ + F^- + F^E, \tag{17}$$

where

$$F^{\pm} = \overline{\overline{U^{\pm}(h+\bar{\bar{\zeta}}+\zeta_{LW}^{\pm})\left[\frac{1}{2}\rho(U^{\pm})^2 + \rho g\left(\bar{\bar{\zeta}}+\zeta_{LW}^{\pm}\right)\right]}}, \tag{18}$$

and F^E is a remainder term (Appendix C) that is negligible over the whole reef compared with $F^{\pm}$ (see Section 3.4). Therefore, incoming and outgoing long waves can be investigated independently.

The energy transfer and frictional dissipation terms of incoming and outgoing long waves are obtained by substituting $U = U^+ + U^-$ into Eqs. (9) and (11),

$$R = R^+ + R^- = -\overline{\overline{U^+\frac{\partial S}{\partial x}}} - \overline{\overline{U^-\frac{\partial S}{\partial x}}}, \tag{19}$$

$$D = D^+ + D^- = -\overline{\overline{U^+\tau_b}} - \overline{\overline{U^-\tau_b}}. \tag{20}$$

2.2.3. Wave height and shape

Significant heights of short and long waves are determined from the potential energy in their frequency bands as $H_{SW} = 4\sqrt{\int_{f_p/2}^{\infty} P(f)\,\mathrm{d}f}$ and $H_{LW} = 4\sqrt{\int_0^{f_p/2} P(f)\,\mathrm{d}f}$, where $P(f)$ is the spectral density of surface elevations.

Skewness (Sk) and asymmetry (As) that represent the lack of symmetry of wave shape relative to horizontal (peaked-ness) and vertical axes (forward or backward pitching) are the major drivers for wave-induced sediment transport, coastal erosion, accretion with and without structure (Pomeroy et al., 2015; Ruessink et al., 2009; Zou and Peng, 2011), and inundation (Cheriton et al., 2016). They are the indicator of wave nonlinearity defined by

$$Sk = \frac{\overline{\overline{\tilde{\zeta}^3}}}{\left(\overline{\overline{\tilde{\zeta}^2}}\right)^{3/2}} \tag{21}$$

$$As = \frac{\overline{\overline{\mathcal{H}\left(\tilde{\zeta}\right)^3}}}{\left(\overline{\overline{\tilde{\zeta}^2}}\right)^{3/2}} \tag{22}$$

where $\tilde{\zeta}$ is the oscillatory surface elevations with zero mean, and $\mathcal{H}(\bullet)$ denotes the Hilbert transform. Skewed waves with $Sk > 0$ have narrow crests and wide troughs, and asymmetric waves with $As < 0$ are characterized by forward pitching forms with steep frontal faces and gentle rear faces.

3. Model results

3.1. Wave height and radiation stress

Cross-reef spatial distributions of short-wave heights (H_{SW}) are displayed in Fig. 2a–d. In Cases B–D, it was assumed that the initial breaking occurred at the highest H_{SW} locations for wave-amplitude reflection coefficients less than 0.07. In Case A, the reflection coefficient was 0.14. Hence, it was assumed that the initial breaking occurred where water depth equaled the incipient breaker depth of Case B because the breaker index was the same for the range of $h_r/H_{SW,0}$ considered here (Yao et al., 2013). Outgoing long-wave heights (H^-_{LW}) started to increase seaward around shoreward ends of the surf zones (Fig. 2e–h) since the breakpoint forcing was the primary source of outgoing long waves. The light-yellow areas in Fig. 2 represent the detected surf zones.

The cross-reef variation of H_{SW} (Fig. 2a–d) was similar to that of previous physical experiments (*e.g.*, Buckley et al., 2018; Liu et al., 2020; Masselink et al., 2019). The transmitted H_{SW} increased with the reef submergence (Cases A–C) and was not sensitive to the forereef slope (Cases B and D). The time-averaged radiation stress ($\bar{\bar{S}}$) increased in the shoaling region due to the enhanced short-wave energy. After that, $\bar{\bar{S}}$ increased in the transition zone just shoreward of the breakpoint, which was most evident in Case D with the milder forereef. It is encouraging to observe that, the non-hydrostatic model SWASH, which theoretically does not resolve the air–water mixture in the surface roller, can qualitatively capture the delay in the decreased radiation stress during roller formation (Svendsen, 1984). The standard deviation of radiation stress ($\sigma(S)$) related to the intensity of bound long wave (Longuet-Higgins and Stewart, 1962) started to decay at the breakpoint.

Cross-reef variations of the total (H_{LW}), incoming (H^+_{LW}), and outgoing (H^-_{LW}) long-wave heights are shown in Fig. 2e–h. H_{LW} increased in the shoaling region, peaked near the breakpoint, then rapidly decreased in a short distance, which was also observed by previous experimental studies (*e.g.*, Buckley et al., 2018; Liu et al., 2021a; Masselink et al., 2019). H^+_{LW} increased in the shoaling region with larger net growth over the milder forereef slope, consistent with Battjes et al. (2004). After that, H^+_{LW} continually increased in the surf zone in all cases though was followed by a gradual decrease over the remainder of the reef flat in Cases A and D. The net growth of H^+_{LW} in the surf zone was larger for lower reef submergence and steeper forereef.

Shoreward of the surf zone, H^-_{LW} was much smaller than H^+_{LW}, with H^-_{LW}/H^+_{LW} being 0.2, 0.08, 0.06, and 0.09 at $x = 2$ m for Cases A–D, respectively (Fig. 2e–h). In the surf zone, H^-_{LW} grew a significant amount. $H^-_{LW,x=x_b}$ was comparable with $H^+_{LW,x=2\,m}$ in Cases A–C. In contrast, $H^-_{LW,x=x_b}$ was smaller than $H^+_{LW,x=2\,m}$ in Case D, implying that (released) bound long waves contributed considerably to the incoming long waves in the surf zone. In the de-shoaling zone (seaward of the surf zone), the decay rate of outgoing long waves as a function of local depth was higher than Green's law for conservative de-shoaling, *i.e.*, wave height ∝ water depth$^{-1/4}$, implying the net energy transfer from outgoing long waves to short waves, despite that they were both free.

3.2. Wave skewness and asymmetry

Short-wave shape underwent significant changes in the shoaling and surf zones (Fig. 3a–d) in a similar fashion to those of regular waves over a low-crested structure (Zou and Peng, 2011) and a reef (Lowe et al., 2019). The shoreward increased positive skewness (Sk) of short waves signified enhanced steep crests and flat troughs due to the generation of higher harmonics and the increased nonlinearity (Chen and Zou, 2018). Asymmetry (As) of short waves was negative, and its magnitude ($|As|$) increased in the shoaling region and outer surf zone, as short waves were becoming pitching forward to trigger breaking. Then, $|As|$ gradually declined in the inner surf zone associated with the wave reformation.

Sk of long waves was negative off the reef (Fig. 3e–h), which denoted the characteristic of bound long waves having deep troughs and flat crests (*e.g.*, Fig. A.14), consistent with the physical experimental data of Masselink et al. (2019) (see Fig. A.13). However, field observation of Cheriton et al. (2016) found $Sk \approx 0$ over the forereef, probably due to the presence of considerable incident free long waves in the field condition. Sk changed to positive values in the surf zone where bound long waves were released and breakpoint-forced long waves were generated. Variation of As of long waves was different from that of short waves. In the shoaling region, As remained nearly zero in Cases A–C (Fig. 3e–g) while increased to 0.5 in Case D (Fig. 3h). Cheriton et al. (2016) also observed positive As over the forereef in some cases. $As > 0$ indicates backward pitching wave forms

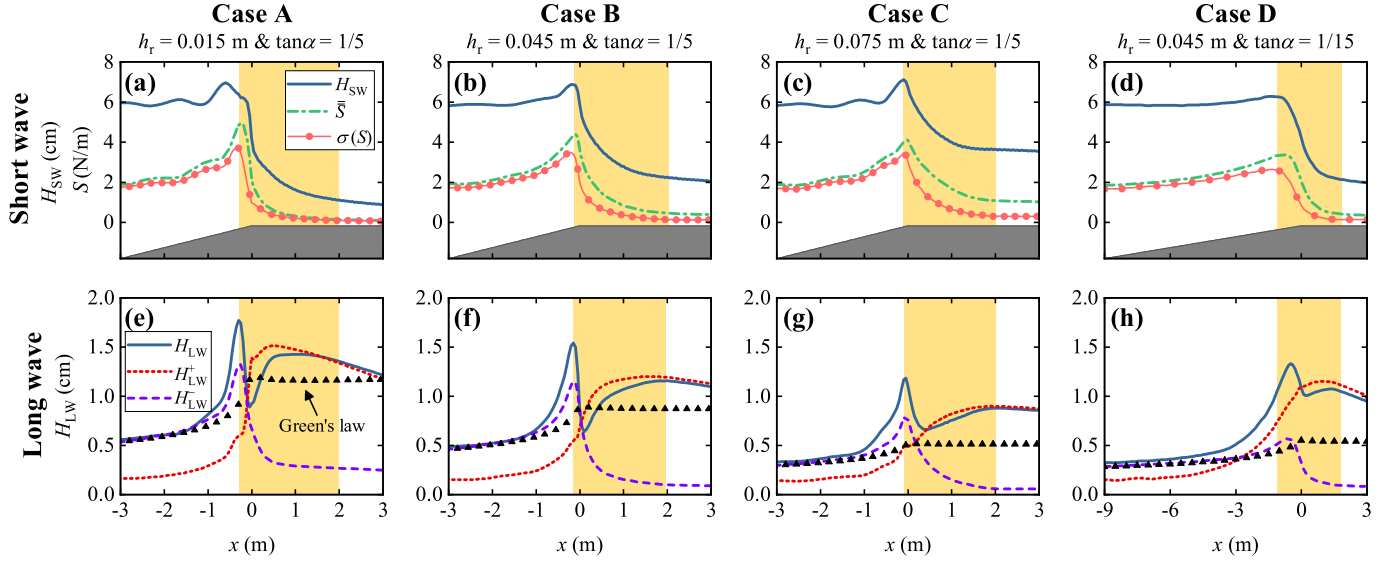

Fig. 2. Cross-reef spatial evolutions of (a)–(d) significant wave height of short waves (H_{SW}), time-averaged radiation stress ($\bar{\bar{S}}$), and standard deviation of radiation stress $\sigma(S)$ calculated by $\sqrt{\frac{1}{N-1}\sum_{i=1}^{N}\left(S_i-\bar{\bar{S}}\right)^2}$ with N the number of data in the time series; (e)–(h) significant heights of total (H_{LW}), incoming (H^+_{LW}), and outgoing (H^-_{LW}) long waves, as well as the Green's law (conservative de-shoaling, wave height ∝ water depth$^{-1/4}$) initiated with H^-_{LW} at the forereef toe. h_r is the reef submergence, and $\tan\alpha$ is the slope of the forereef. The light-yellow area indicates the surf zone, and the gray area illustrates the reef topography.

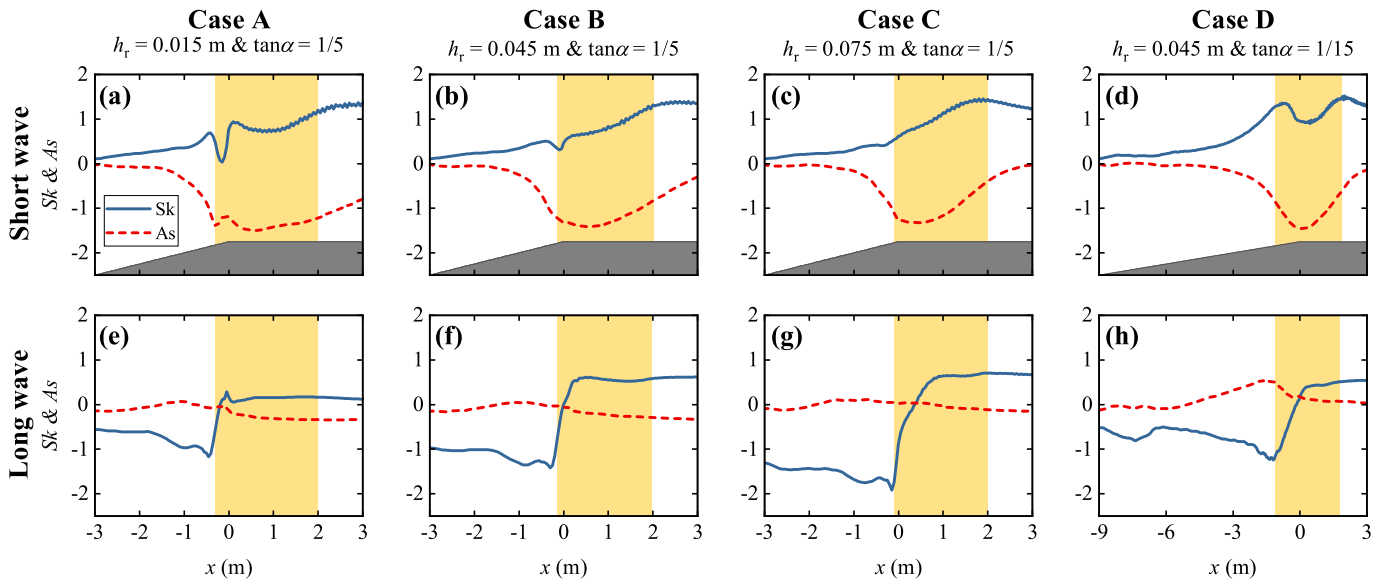

Fig. 3. Skewness (Sk, Eq. (21)) and asymmetry (As, Eq. (22)) of (a)–(d) short-wave and (e)–(h) long-wave surface elevations. $Sk > 0$ indicates waves with narrow crests and wide troughs, and $As < 0$ indicates forward pitching waves with steep frontal faces and gentle rear faces. h_r is the reef submergence, and $\tan\alpha$ is the slope of the forereef. The light-yellow area indicates the surf zone, and the gray area illustrates the reef topography.

with gently sloping front faces and steep rear faces, which may be a characteristic of bound long wave over a sloping bottom. We confirmed the rationality of $As > 0$ using the nearly resonant solution of bound long wave proposed by Liao et al. (2021) (not shown). Over the reef flat, long waves evolved into forward pitching forms in Cases A–C with $As < 0$, and became symmetric in Case D with $As \approx 0$.

3.3. Cross-correlation between long waves and radiation stress

To reveal the generation mechanism of long waves, cross-correlation between long-wave surface elevations along the reef ($\zeta_{LW}(x,t)$) and radiation stress at the forereef toe ($S(x_{toe},t)$) is shown in Fig. 4a–d ($x_{toe} = -3$ m in Cases A–C and $x_{toe} = -9$ m in Case D). In the shoaling region, the negative cross-correlation from the forereef toe at zero time lag ($t_{lag} = 0$) up to the breakpoint at a positive time lag ($t_{lag} > 0$) indicates incoming bound long waves. Another stronger negative bar originated from the breakpoint and propagated seaward due to the generation of outgoing breakpoint-forced long waves. In the surf zone, the evolution pattern of cross-correlation signal depended on the reef submergence and the forereef slope. The change of cross-correlation from negative to positive values was rapid in Cases A–B, which implied a sudden transition from a bound long wave dominated low-frequency wave field to a breakpoint-forced long wave dominated one. However, the transition was slower and incompleted in Cases C–D. A small part of the negative bar passed through the reef edge behind the strong positive bar that arose from the reef edge, signifying co-existing (released) bound and breakpoint-forced long waves.

The change of short-wave group structure was detected by the cross-correlation between radiation stresses along the reef ($S(x,t)$) and that at the forereef toe ($S(x_{toe},t)$) (Fig. 4e–h). Short-wave group propagated shoreward without significant changes in its structure up to the breakpoint. In the surf zone, the positive bar indicates that the group structure largely remained during depth-limited breaking, which is different from the inversion of group structure over a sandy beach (Janssen et al., 2003). We ascribed the positive bar to the generation of strong breakpoint-forced long wave in phase with the wave group, which modifies the local water depth of short waves. Large and small short waves are allowed to enter the shallow reef flat on the crest and trough of the breakpoint-forced long wave, respectively. The depth modulation by long wave over the reef flat is more significant in the case of low reef submergence. This can also explain the negative cross-correlation bar observed in Cases C–D induced by the released bound long waves. Liu and Li (2018) demonstrated a linear dependence of groupiness in inner reef on the ratio of long-wave height to mean water depth.

Since short-wave groups and long waves were deformed in the surf zone, it is necessary to inspect the cross-correlation between collocated long-wave surface elevations ($\zeta_{LW}(x,t)$) and radiation stress ($S(x,t)$). Fig. 4i–l show that the incoming long waves ($\zeta^{+}_{LW}(x,t)$) were inversely related to the local $S(x,t)$ with a positive time lag in the shoaling zone due to the presence of non-equilibrium bound long wave in quadrature with the short-wave group (Liao et al., 2021). Time lag at the breakpoint was almost the same in Cases A–C but was larger in Case D. In the surf zone, two factors influence the cross-correlation between $\zeta^{+}_{LW}(x,t)$ and $S(x,t)$. Firstly, long-wave crests consisting of positive parts of bound long waves and free long waves radiated ahead of short-wave groups are generated around the breakpoint. These crests are higher over a milder slope and are positively cross-correlated with local short-wave groups at negative time lag (Lara et al., 2011). Secondly, incoming breakpoint-forced long waves have a small positive time lag to the short-wave groups (Contardo et al., 2018), which is more evident over a steeper bottom (Baldock, 2012). Therefore, the negative time lag of $\zeta^{+}_{LW}(x,t)$ to $S(x,t)$ shortly behind the breakpoint was smallest in Case A and largest in Case D. Finally, the time lag was positive after short-wave breaking for all cases. Transformations of short-wave groups and incoming long waves over the reef are illustrated in Fig. 5.

At the breakpoint, the outgoing long-wave surface elevations ($\zeta^{-}_{LW}(x,t)$) were negatively correlated to but lagged behind ($t_{lag} > 0$) the local radiation stress ($S(x,t)$) (Fig. 4m–p), in agreement with the theory of Contardo et al. (2018). Seaward of the breakpoint, although $\zeta^{-}_{LW}(x,t)$ and $S(x,t)$ freely propagated in opposite directions, they were still strongly correlated, allowing energy exchange between them.

3.4. Long-wave energy balance

Cross-reef variations of long-wave energy flux (F), flux gradient ($\partial F/\partial x$), rate of work done by the radiation-stress gradient (R), and dissipation rate due to bottom friction (D) are shown in Fig. 6 to gain insight in the long-wave evolution. Since the remainder term in separating incoming and outgoing long-wave energy fluxes was negligible ($|F^{E}| \ll |F^{\pm}|$), F was a linear superposition of incoming (F^{+}) and outgoing (F^{-}) fluxes (Fig. 6a–d). $\partial F^{+}/\partial x > 0$ indicates an increase

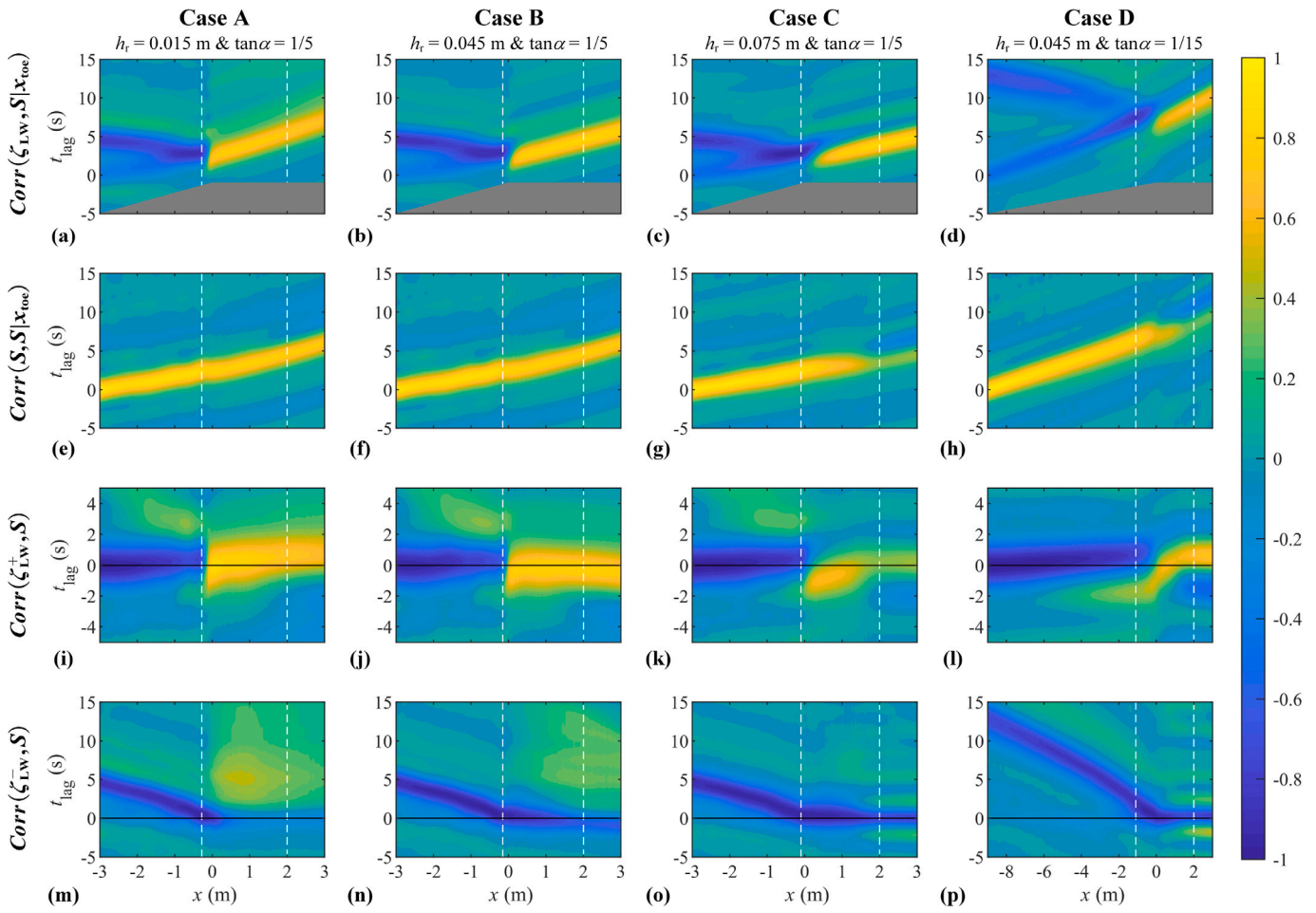

Fig. 4. Cross-correlation between (a)–(d) long-wave surface elevations along the reef $\zeta_{LW}(x,t)$ and radiation stress at the forereef toe $S(x_{toe},t)$; (e)–(h) radiation stresses along the reef $S(x,t)$ and at the forereef toe $S(x_{toe},t)$; (i)–(l) incoming long-wave surface elevations along the reef $\zeta^+_{LW}(x,t)$ and *collocated* radiation stress $S(x,t)$; (m)–(p) outgoing long-wave surface elevations along the reef $\zeta^-_{LW}(x,t)$ and *collocated* radiation stress $S(x,t)$. The cross-correlation between $A(t)$ and $B(t)$ is defined by $Corr(A,B) = \overline{A(t+\tau)B(t)}/[\sigma(A(t))\sigma(B(t))]$, where $\sigma(\bullet)$ denotes the standard deviation. h_r is the reef submergence, and $\tan\alpha$ is the slope of the forereef. The gray area illustrates the reef topography. The two vertical white dashed lines denote the surf-zone edges.

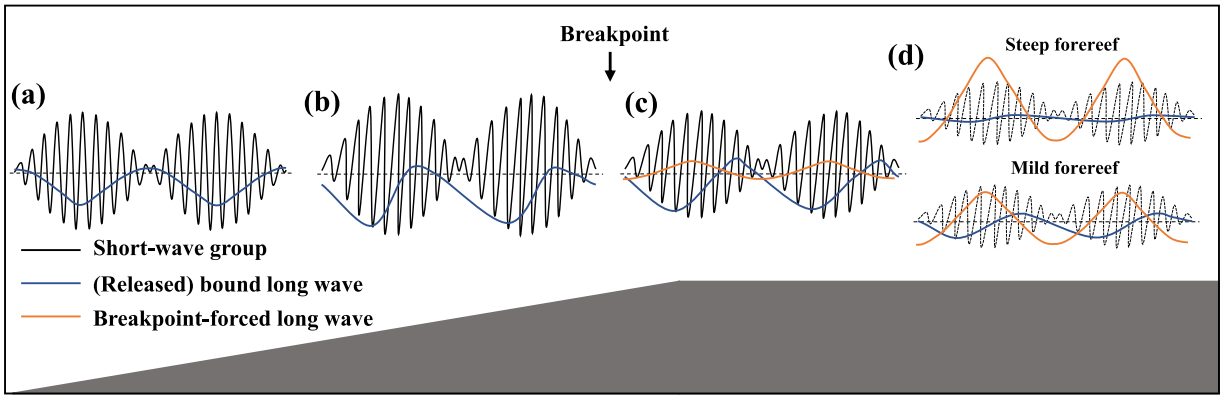

Fig. 5. Sketches of incoming long waves generated by bound long wave and breakpoint-forced long wave mechanisms. (a) Bound long wave in antiphase with the short-wave group. (b) Bound long wave lagging behind the short-wave group. (c) Decaying (released) bound long wave and growing breakpoint-forced long wave. (d) Upper: weak (released) bound long wave and dominant breakpoint-forced long wave; Lower: co-existing (released) bound and breakpoint-forced long wave; the dotted curve denotes the imaginary short-wave group without significant deformation during breaking. The gray area illustrates the reef topography. This conceptual graphical description is inspired by the conceptual sketch of long wave evolution over a sloping beach by Brocchini (2020) and De Bakker et al. (2016a).

in $|F^+|$ in the positive x-direction, and $\partial F^-/\partial x > 0$ means an increase in $|F^-|$ in the *negative* x-direction because $F^- < 0$. To sum up, $\partial F/\partial x > 0$ always reflects an energy-flux enhancement in the direction of wave propagation and vice versa. Similarly, $R > 0$ indicates a nonlinear energy transfer from short to long waves, and $R < 0$ suggests the inverse transfer, irrelevant to the wave direction.

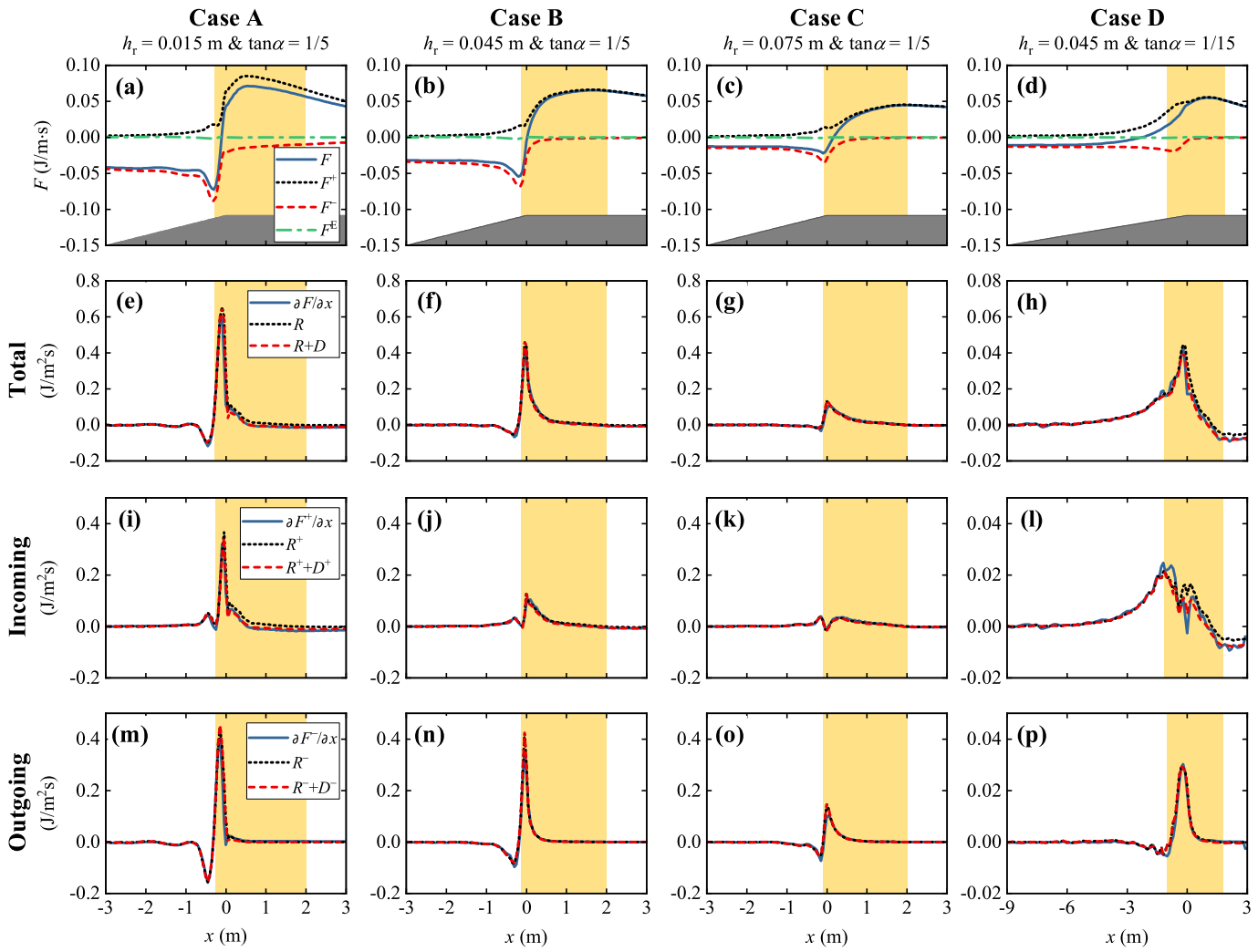

Fig. 6. Cross-reef variations of (a)–(d) total(F), incoming (F^+), and outgoing (F^-) long-wave energy fluxes, as well as the remainder term ($F^E = F - F^+ - F^-$). Cross-reef variations of energy-flux gradient ($\partial F/\partial x$), the rate of work done by the radiation-stress gradient (R), and the frictional dissipation rate (D) for (e)–(h) total, (i)–(l) incoming, and (m)–(p) outgoing long waves. h_r is the reef submergence, and $\tan\alpha$ is the slope of the forereef. The light-yellow area indicates the surf zone, and the gray area illustrates the reef topography.

3.4.1. *Total long wave*

Over the whole reef, $\partial F/\partial x$ was mainly balanced by R (Fig. 6e–h), proving that the nonlinear interaction with short waves is responsible for the generation and dissipation of long waves. The discernible mismatch between $\partial F/\partial x$ and R in Case A could be mostly compensated by D (Fig. 6e). Although D was small in Case A, its accumulation along the reef flat was substantial in reducing F for $x > 0.5$ m (Fig. 6a). D was not evident in the other cases because the frictional shear stress is inversely proportional to the water depth to the power of 1/3 in the simulation (Eq. (5)). Pomeroy et al. (2012) also demonstrated more significant friction at lower tidal levels in field conditions. The energy transfer pattern in Case D (Fig. 6h) was similar to that over a 1/30 plane slope obtained using a fully-nonlinear stochastic analysis (Rijnsdorp et al., 2022). It should be noted that the energy balance described in Eq. (6) was still not perfect, possibly due to the error in post-process calculating $\partial S/\partial x$ (da Silva et al., 2021).

Van Dongeren et al. (2007) suggested that long waves may break over a mild bottom in very shallow water where short waves have been almost dissipated, with the incipient breaking detected by an index of long-wave height to water depth ratio. In Case A, $H^+_{LW}/(h+\bar{\bar{\zeta}})$ decreased from 0.68 at $x = 0$ m to 0.44 at $x = 3$ m, and $H_{LW}/(h+\bar{\bar{\zeta}})$ decreased from 0.52 at $x = 0.5$ m to 0.45 at $x = 3$ m. Both ratios exceeded the breaker index (~ 0.44) suggested by Van Dongeren et al. (2007). However, long waves were unlikely to break over the reef flat considering the excellent agreement between $\partial F/\partial x$ and $R + D$ (Fig. 6e) and the small $|As|$ (Fig. 3e). We suspect that the presence of considerable short waves suppressed the self-interaction of long waves.

3.4.2. *Incoming and outgoing long waves*

Results show that short waves always transferred energy to incoming long waves along the reef ($R^+ > 0$), except for $x > 1.5$ m in Case D where $R^+ < 0$ (Fig. 6i–l). In the shoaling region, R^+ depended on the forereef slope but was not sensitive to the reef submergence. Although maximum R^+ was smaller over the milder forereef (Case D), the integral of R^+ was higher because the milder forereef provided more ample space for the accumulation of energy transfer during shoaling (Li et al., 2020). In the surf zone, the maximum R^+ had a larger value given smaller h_r, suggesting that the energy transfer was intense under violent short-wave breaking. Notably, the integral of R^+ in the surf zone was always positive. It is therefore concluded that the generation of incoming breakpoint-forced long waves dominates over the dissipation of bound long waves, which contradicts the speculation in previous studies (Buckley et al., 2018; Liu et al., 2021a) and the results of weakly nonlinear analysis (Péquignet et al., 2014).

According to the theoretical model by Contardo et al. (2018), efficiencies of the breakpoint-forcing mechanism in generating incoming and outgoing long waves are almost the same. In other words, in the surf zone, the net increment in $|F^-|$ (*i.e.*, $|\Delta F^-|$) approximately equals

the net increment in $|F^+|$ (*i.e.*, $|\Delta F^+|$). Nevertheless, Fig. 6a–d show that $\left(|\Delta F^-| - |\Delta F^+|\right)/|\Delta F^-|$ was 0.41, 0.25, 0.09, and 0.16 in Cases A–D, respectively. $|\Delta F^+| < |\Delta F^-|$ was caused by the energy transfer from incoming bound long waves to short waves and the frictional dissipation (Fig. 6i–l). However, because incoming bound long waves partially contributed to the incoming long waves over the reef flat, $|F^+|$ at the end of the surf zone (*i.e.*, $|F^+|_{x=2\,\mathrm{m}}$) was comparable with or even larger than $|F^-|$ at the breakpoint (*i.e.*, $|F^-|_{x=x_b}$) in Cases B–D, where the effect of bottom friction was not considerable. Assuming that the enhancements of incoming and outgoing breakpoint-forced long waves were the same in the surf zone, the ratio of incoming (released) bound long wave energy flux to incoming breakpoint-forcing long wave energy flux at $x = 2$ m could be roughly estimated by $\left(|F^+|_{x=2\,\mathrm{m}} - |\Delta F^-|\right)/|\Delta F^-|$, being −0.15, −0.03, 0.32, 1.63 in Cases A–D, respectively. The negative ratio in Case A was caused by the bottom friction, while the nearly zero and positive ratios in Cases B–D indicated an increased contribution from (released) bound long waves, in line with the cross-correlation analysis (Fig. 4a–d).

At the breakpoint, $|F^-|$ peaked (Fig. 6a–d) as R^- approached zero (Fig. 6m–p). After that, $|F^-|$ decreased seaward in the de-shoaling zone, which was well balanced by the negative R^-, making the de-shoaling rate of H_{LW}^- larger than Green's law. The underlying mechanism will be discussed further in Section 5.2.

4. Linear and weakly nonlinear analyses

The above fully nonlinear analysis requires the input of horizontal-velocity profile from the bottom to the free water surface (Eq. (8)), which is challenging to measure in laboratory experiments and field observations. Usually, time series of velocity at a fixed submerged point is available (*e.g.*, Buckley et al., 2018; De Bakker et al., 2016b; Pomeroy et al., 2012; Péquignet et al., 2014; Zheng et al., 2020; Zou et al., 2003), and the long-wave velocity U is derived as,

$$U = \overline{u} - \overline{\overline{u}}. \tag{23}$$

Similarly, some other studies (*e.g.*, Lashley et al., 2020; Liu et al., 2021a; Yao et al., 2020) used the depth-averaged velocity u_{avg} from numerical models to calculate U as,

$$U = \overline{u_{\mathrm{avg}}} - \overline{\overline{u_{\mathrm{avg}}}}. \tag{24}$$

U defined by Eq. (23) was adopted in the weakly nonlinear long-wave energy balance equation of Henderson et al. (2006) assuming small-amplitude short waves and smaller long waves. A modified form has been applied to a coral reef (Péquignet et al., 2014) and sandy beaches (*e.g.*, Rijnsdorp et al., 2015),

$$\frac{\partial F_{\mathrm{WNL}}(f)}{\partial x} = R_{\mathrm{WNL}}(f), \tag{25}$$

where R_{WNL} is the frequency-dependent energy transfer term,

$$R_{\mathrm{WNL}}(f) = -C_{U,\partial S/\partial x}(f), \tag{26}$$

with C the co-spectrum. F_{WNL} is the weakly nonlinear energy flux containing a linear term (F_{L}) and a nonlinear correction (F_{S}, induced by Stokes transport), *i.e.*,

$$F_{\mathrm{WNL}}(f) = F_{\mathrm{L}}(f) + F_{\mathrm{S}}(f), \tag{27}$$

with

$$F_{\mathrm{L}}(f) = \rho g(h + \overline{\zeta})C_{\zeta_{\mathrm{LW}},U}(f), \tag{28}$$

$$F_{\mathrm{S}}(f) = \rho g C_{\zeta_{\mathrm{LW}},\zeta_{\mathrm{SW}}u_{\mathrm{SW}}}(f). \tag{29}$$

$u_{\mathrm{SW}} = u - \overline{u}$ is an approximation of short-wave velocity in line with Eq. (23).

Integral of Eq. (28) over the low-frequency band (0–$f_{\mathrm{p}}/2$) is identical to Eq. (7) as long as U determined by Eq. (23) is used for both of them. Accordingly, the linear energy flux for incoming and outgoing long waves ($F_{\mathrm{L}}^{\pm}$) can be calculated using Eq. (18) in combination with Eq. (23), which is equivalent to Sheremet et al. (2002, Eqs. (2)–(3)). Considering the linear property of co-spectrum, we may further divide F_{S} into incoming and outgoing components,

$$F_{\mathrm{S}}^{\pm} = \rho g C_{\zeta_{\mathrm{LW}}^{\pm},\zeta_{\mathrm{SW}}u_{\mathrm{SW}}}(f). \tag{30}$$

The above linear and weakly nonlinear analysis methods may lead to significant errors in a highly-nonlinear environment over a shallow reef, which has not been assessed previously.

4.1. Separation of incoming and outgoing long waves

Surface elevations of incoming and outgoing long waves were separated using Eq. (13) with U defined differently by Eqs. (8), (23), and (24). Compared with H_{LW}^+ with Eq. (8), Eq. (23) resulted in an overestimation of H_{LW}^+ in the shoaling and outer surf zones, followed by an underestimation over the remainder of the reef flat (Fig. 7a–d). The degree of overestimation depended more on the forereef slope than the reef submergence, with maximum overestimation rates of ~100% in Cases A–C and ~60% in Case D. Inversely, the rate of underestimation in the inner surf zone was sensitive to the reef submergence, being 27%, 12%, 6%, and 10% at $x = 2$ m in Cases A–D, respectively. Notably, similar to previous studies (Buckley et al., 2018; Liu et al., 2021a), there was a non-physical decrease in H_{LW}^+ with Eq. (23) shortly behind the breakpoint. Incoming long waves do reduce in amplitude following short-wave breaking over a mild slope where breakpoint-forced long waves are negligible (Baldock, 2012), but this is not the case for the coral reef because the generation of breakpoint-forced long waves compensates for the dissipation of bound long waves (Section 3.4).

H_{LW}^- with Eqs. (8) and (23) were enhanced seaward in the surf zone with different increments (Fig. 7e–h). After that, they diverged significantly in the de-shoaling region. Eq. (8) resulted in a de-shoaling rate of H_{LW}^- larger than Green's law, indicating the energy transfer from outgoing long waves to short waves, whereas the de-shoaling rate with Eq. (23) was lower than Green's law. As for Eq. (24), the errors in separating $H_{\mathrm{LW}}^{\pm}$ were smaller than those with Eq. (23), but still considerable. Nevertheless, it is unnecessary to use Eq. (24) when u_{avg} is known because u_{avg} applies to Eq. (8), *i.e.*, $U = \overline{u_{\mathrm{avg}}(h+\zeta) - Q_{\mathrm{c}}}\Big/(h+\overline{\zeta})$, with $Q_{\mathrm{c}} = \overline{\overline{u_{\mathrm{avg}}(h+\zeta)}}$.

4.2. Weakly nonlinear analysis

Case B was used as an example to assess the accuracy of weakly nonlinear balance analysis results (Fig. 8). For $x < 0.1$ m, F_{S} was negative because both ζ_{LW}^+ and ζ_{LW}^- were negatively correlated to the local short-wave group (Fig. 4j and n). Rijnsdorp et al. (2015) found a much smaller $|F_{\mathrm{S}}|$ than $|F_{\mathrm{L}}|$ over a sandy beach, while for the reef, $|F_{\mathrm{S}}| > |F_{\mathrm{L}}|$ and $|F_{\mathrm{S}}^+| \approx |F_{\mathrm{L}}^+|$ prior to short-wave breaking (Fig. 8a–b), owing to the large breaker index over the steep forereef. In this sense, the Stokes-transport correction was vital, but the deviation of F_{WNL} from F_{FNL} (fully-nonlinear energy flux, Eq. (7)) was still significant. By separately inspecting incoming and outgoing long waves (Fig. 8b–c), it was found that the discrepancies between F_{WNL} and F_{FNL} in the shoaling region and the inner surf zone were mainly caused by outgoing and incoming long waves, respectively. In both regions, the corresponding ratios of long-wave height to water depth were typically large (Fig. 8h–i), therefore, the long-wave modulation of local water depth was significant, which infringes the assumption of small-amplitude long waves. This point will be discussed further in Section 5.1. The balances between the weakly nonlinear energy transfer term (R_{WNL}) and the linear and weakly nonlinear energy-flux gradients ($\partial F_{\mathrm{L}}/\partial x$ and $\partial F_{\mathrm{WNL}}/\partial x$) integrated over the long-wave frequency band were poor. Notably, for total and incoming long waves, R_{WNL} was negative shortly behind the breakpoint, suggesting that energy was transferred to short waves, whereas the actual transfer direction was the opposite (Fig. 6f and j). The unbalance of Eq. (25) over the reef is due to that R_{WNL} ignores the contributions of Stokes transport and long-wave modulation of water depth under the assumed ordering.

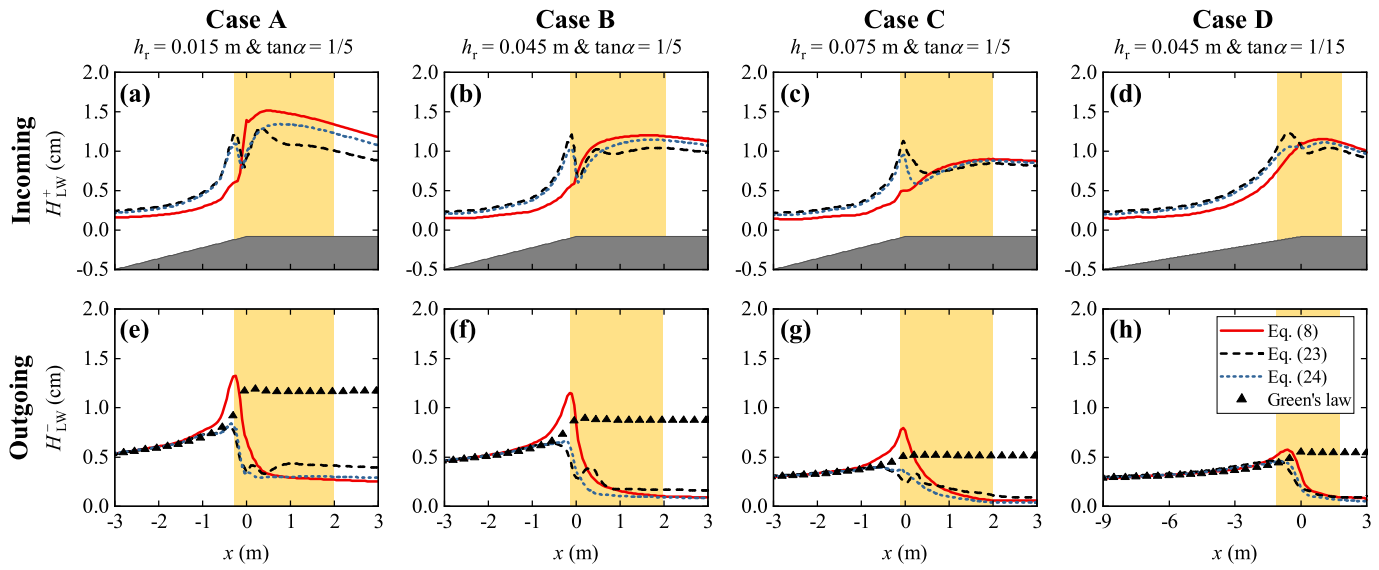

Fig. 7. Comparisons between (a)–(d) incoming (H^+_{LW}) and (e)–(h) outgoing (H^-_{LW}) long-wave significant heights calculated based on different approaches for extracting depth-averaged low-frequency velocity, *i.e.*, $U = \overline{\int_{-h}^{\zeta} u\,dz - Q_c}/(h+\overline{\zeta})$ (Eq. (8)), $U = \overline{u} - \overline{\bar{u}}$ (Eq. (23)), and $U = \overline{u_{avg}} - \overline{\overline{u_{avg}}}$ (Eq. (24)). Green's law denoted by triangles (conservative de-shoaling, wave height $\propto$ water depth$^{-1/4}$) is initiated with H^-_{LW} at the forereef toe. h_r is the reef submergence, and $\tan\alpha$ is the slope of the forereef. The light-yellow area indicates the surf zone, and the gray area illustrates the reef topography.

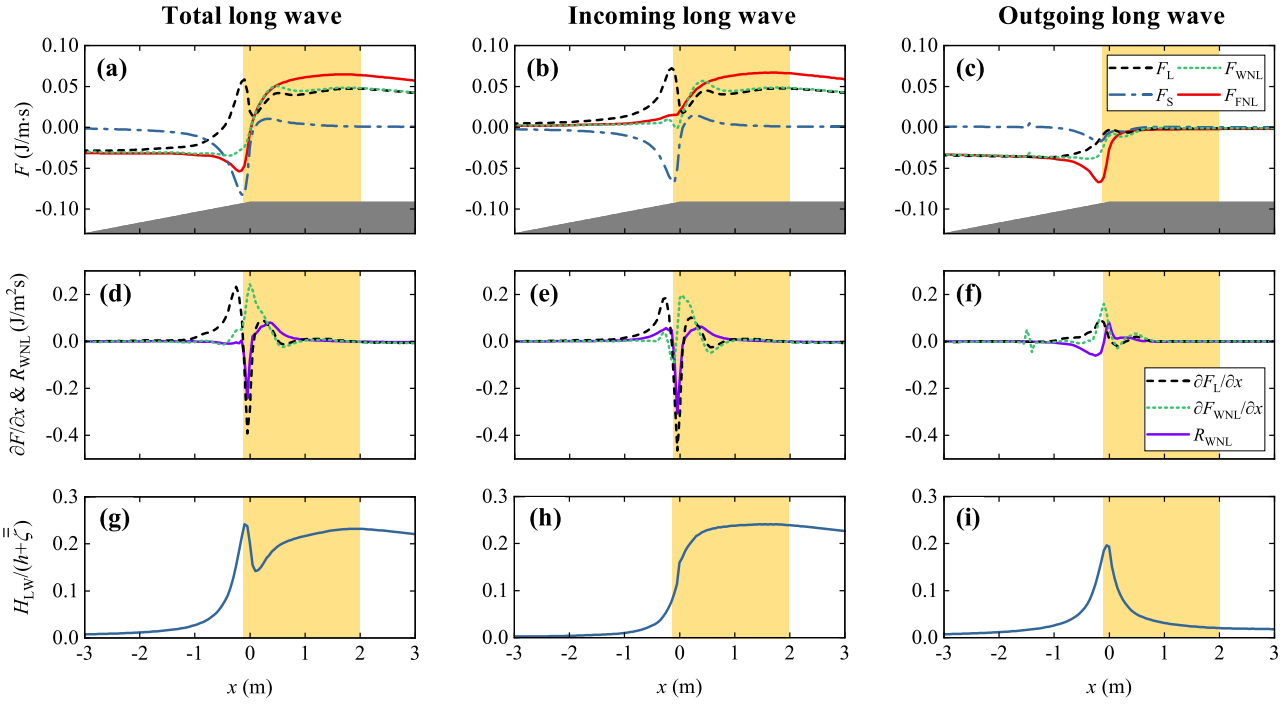

Fig. 8. (a)–(c) Comparisons between long-wave energy fluxes calculated by linear (F_L, Eq. (28)), Stokes-drift correction (F_S, Eq. (29)), weakly nonlinear ($F_{WNL} = F_L + F_S$, Eq. (27)), and fully nonlinear (F_{FNL}, Eq. (7)) analysis methods, integrated over the spectrum; (d)–(f) Comparisons between energy-flux gradients (F_L and F_{WNL}) and nonlinear energy transfer (R_{WNL}, Eq. (25)) integrated over the spectrum; (g)–(i) Ratio of long-wave height to mean water depth. Case B, h_r = 0.045 m and $\tan\alpha$ = 1/5, where h_r is the reef submergence, and $\tan\alpha$ is the slope of the forereef. The light-yellow area indicates the surf zone, and the gray area illustrates the reef topography.

5. Discussion

5.1. Extracting long-wave velocity with mass conservation

Results of the present study emphasize that the long-wave velocity U must be extracted from the whole velocity profile with mass conservation satisfied, as defined by $U = \overline{\int_{-h}^{\zeta} u\,dz - Q_c}/(h+\overline{\zeta})$ (Eq. (8)). Only in this method, U includes both the two crucial nonlinear terms in the low-frequency flux, (a) the Stokes transport at the group scale related to $\overline{\int_{\bar{\zeta}}^{\zeta} u\,dz}$ and (b) the nonlinear low-frequency orbital velocity due to long-wave modulation of local water depth related to $\overline{\int_{-h}^{\bar{\zeta}} u\,dz}$. The conventional method of extracting U from the low-pass filtered single-point velocity ($U = \overline{u} - \overline{\bar{u}}$, Eq. (23)) and the low-pass filtered depth-averaged velocity ($U = \overline{u_{avg}} - \overline{\overline{u_{avg}}}$, Eq. (24)) in previous studies lead to significant errors (Figs. 7–8) due to the assumptions involved therein. Eq. (23) considers neither of the nonlinear terms because it

implicitly assumes $H_{SW}/(h+\bar{\bar{\zeta}}) \ll 1$ and $H_{LW}/(h+\bar{\bar{\zeta}}) \ll 1$. Eq. (24) may partially include the nonlinear terms, and the $H_{LW}^{\pm}$ calculated with Eq. (24) is closer to the accurate $H_{LW}^{\pm}$ by Eq. (8) than by Eq. (23) (Fig. 7). The important contribution of the nonlinear low-frequency energy flux induced by Stokes transport was recognized by the weakly nonlinear analysis of Henderson et al. (2006). The present study further show that neglecting the stokes transport in mass flux leads to a significant overestimation of energy flux of incoming long waves (Fig. 8b) and therefore the overestimation of incoming long-wave height prior to breaking (Fig. 7b).

In addition, neglecting the long-wave modulation of local water depth assuming $H_{LW}/(h+\bar{\bar{\zeta}}) \ll 1$ also introduces considerable errors over a shallow reef. The depth-integrated mass conservation equation for long wave,

$$\frac{\partial \zeta_{LW}}{\partial t} + \frac{\partial (h+\bar{\zeta})U}{\partial x} = 0, \tag{31}$$

is nonlinear since $\bar{\zeta} = \bar{\bar{\zeta}} + \zeta_{LW}$. Assuming $H_{LW}/(h+\bar{\bar{\zeta}}) \ll 1$, the equation is linearized, leading to $\overline{\overline{U}} = 0$, as in Eqs. (23)–(24). However, taking time-averaging of Eqs. (14) and (31) yields,

$$\overline{\overline{U^{\pm}}} = \mp \frac{1}{h+\bar{\bar{\zeta}}} \times \overline{\overline{\frac{c^{\pm}}{h+\bar{\zeta}} \left(\zeta_{LW}^{\pm}\right)^2}}, \tag{32}$$

which indicates that $\overline{\overline{U^+}} < 0$, $\overline{\overline{U^-}} > 0$, and $\overline{\overline{U}}$ is of order $O\left(H_{LW}/(h+\bar{\bar{\zeta}})\right)^2$ for progressive waves.

Fig. 9a shows that the magnitude of $\overline{\overline{U}}$ rapidly increases with the increasing $H_{LW}/(h+\bar{\bar{\zeta}})$. $\overline{\overline{U}} > 0$ indicates $H_{LW}^{-} > H_{LW}^{+}$, and $\overline{\overline{U}} < 0$ indicates $H_{LW}^{+} > H_{LW}^{-}$, agreeing with Fig. 9b. Assuming $\overline{\overline{U}} = 0$ for the region where $H_{LW}^{-} > H_{LW}^{+}$ would lead to the underestimated outgoing long waves, *e.g.*, $-1 < x < 0.2$ m in Case B (Figs. 7f and 8c), even though the Stokes correction is considered. Similarly, assuming $\overline{\overline{U}} = 0$ for the region where $H_{LW}^{+} > H_{LW}^{-}$ would lead to the underestimated incoming long waves, *e.g.*, $x > 0.5$ m in Case B (Figs. 7b and 8b).

5.2. Energy transfer between short and long waves

Whether the product term $-U\,(\partial S/\partial x)$ represents the work done by radiation-stress gradient on free or bound long waves remains an open question (Moura and Baldock, 2019). Some researchers applied this term to bound long wave (*e.g.*, Battjes et al., 2004; Henderson et al., 2006), while Baldock (2012) interpreted U as the velocity of free long wave. We believe that U can represent the velocities of both of them since Phillips (1977) and Schäffer (1993) derived the energy transfer term without requiring that U must be induced by a free or a bound long wave, as long as $U(h+\bar{\zeta})$ equals the low-frequency mass flux and has a much longer period than that of short waves. Excellent balances between $\partial F^{+}/x$ and R^{+} in the shoaling region and the surf zone demonstrated in Fig. 6i–l support this viewpoint.

It is well accepted that energy transfer between free waves is weak, and therefore, a substantial energy transfer between long and short waves in the surf zone occurs only if the long wave is nonlinearly bounded to the short-wave group. However, we think substantial energy transfer between free waves may occur under certain phase coupling between them, for example, the sustained phase coupling between short-wave groups and incoming free breakpoint-forced long waves (Contardo et al., 2018). Accordingly, long waves do not necessarily remain bound to transfer energy to short waves. Resonant wave interaction occurs as long as their phase relationship remains almost constant in the case that the group celerity approaches the shallow-water wave celerity.

Another example is the substantial energy transfer from outgoing free breakpoint-forced long waves to incoming short waves in intermediate water seaward of the surf zone, as captured by $-U\,(\partial S/\partial x)$ in Fig. 6m–p. Although possible energy transfer between outgoing free long waves and incoming short waves was initially proposed by Battjes et al. (2004) over a mild slope, the energy transfer direction was not consistent at all discrete frequencies in their cases, resulting in a zero integrated energy transfer rate over the frequency band, which led to the question about its reality (Van Dongeren et al., 2007). We propose that the energy transfer at discrete frequencies is true, and a substantial net transfer requires the phase coupling between outgoing long waves and incoming short-wave groups to be consistent at all discrete frequencies. Waves in Battjes et al. (2004) did not meet this requirement because the outgoing long waves were mostly the reflected ones released from bound long waves. Although the incoming bound long waves were close to being in antiphase with local short-wave groups at all frequencies at the breakpoint (Battjes et al., 2004, Figure 6), the phase changes of long waves at various frequencies deviated from each other as they propagated towards the shoreline and back to

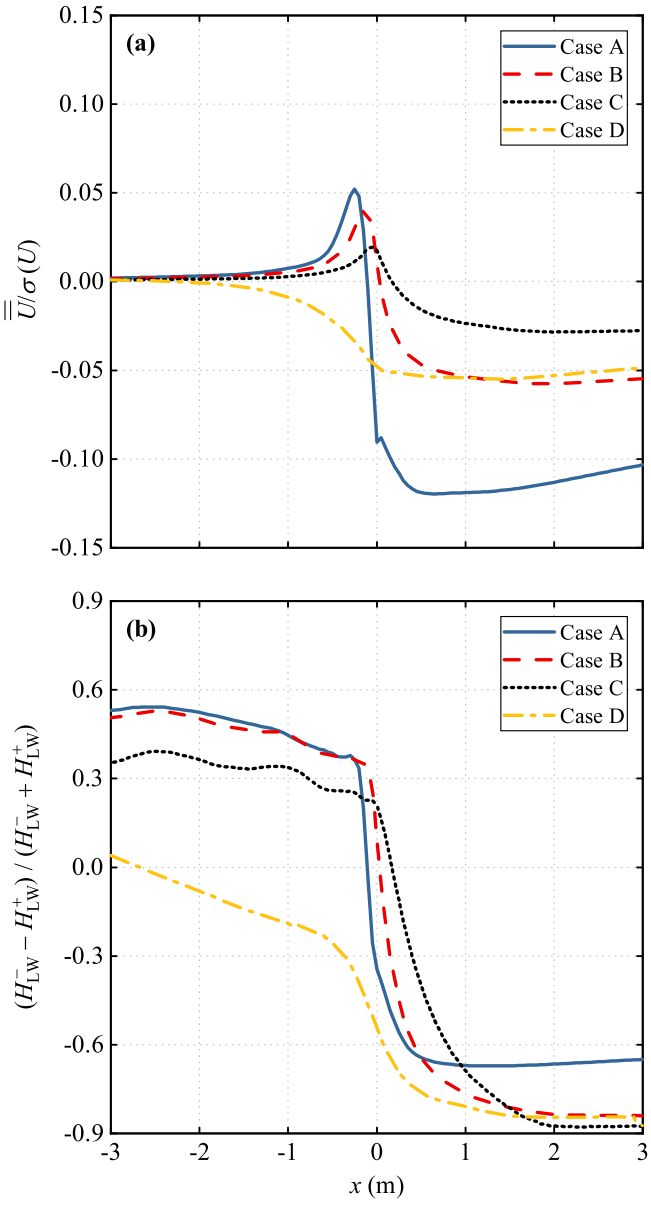

Fig. 9. Spatial variations of (a) the ratios of time averages $\overline{\overline{(\bullet)}}$ to standard deviations $\sigma(\bullet)$ of long-wave velocity U (Eq. (8)) over the reef for Cases A–D (see Table 1); (b) Differences between outgoing and incoming long-wave heights ($H_{LW}^{-} - H_{LW}^{+}$) normalized by the sums of outgoing and incoming long-wave heights ($H_{LW}^{-} + H_{LW}^{+}$).

the breakpoint due to variation of wavenumbers of these long waves. As a result, the phase differences between outgoing long waves and group forcing at the breakpoint were distributed between $-\pi$ to π (Battjes et al., 2004, Figure 7), so that the net energy transfer in the overall low-frequency band was minimal. Here, in this study over the reef, the outgoing long waves were directly generated by the moving breakpoint forcing in the surf zone. It follows that the phase differences with the group forcing at the breakpoint were similar at all frequencies, varying slightly from -0.98π at 0.02 Hz to -0.76π at 0.30 Hz for Case B as an example (Fig. 10a–b), in qualitative agreement with the theoretical solution of Contardo et al. (2018, Figure 3b). Within a short distance seaward of the breakpoint, the phase differences at these frequencies remained within the same quadrant ($-\pi < \Delta\phi < -0.5\pi$) (Fig. 10a–b), allowing consistent and sustained energy transfer from outgoing long waves to incoming short waves ($R^- < 0$) (Fig. 10c–d).

5.3. Effects of reef-flat submergence

Previous studies revealed the influence of bottom slope on long-wave evolution using wave data over broadly uniform bottoms rising to dry shores (*e.g.*, Battjes et al., 2004; Baldock, 2012; De Bakker et al., 2016b; Padilla and Alsina, 2018). For a reef topography with an abrupt slope change at the reef edge, the present study suggests that, besides the forereef bottom slope, the reef-flat submergence affects the type and intensity of long waves through energy exchange between long and short waves. This finding is also an addition to previous works that largely focused on the influence of reef submergence on frictional long-wave dissipation over a shallow reef flat (*e.g.*, Pomeroy et al., 2012; Van Dongeren et al., 2013).

In the shoaling region, shoreward increasing radiation stress does positive work on bound long waves. By inference, when the radiation stress rapidly decreases (Fig. 2a–d) and the short-wave group structure does not significantly change in the outer surf zone (Fig. 4e–h), the radiation stress does substantial negative work on bound long waves regardless of whether the bound waves have been released, therefore, causing the decay of the bound waves. Meanwhile, the moving breakpoint forces strong free waves so that the net energy transfer R^+ is a compromise between energy transfers from incoming (released) bound long waves to short waves and from short waves to incoming breakpoint-forced long waves in the surf zone. This addresses the question raised by Masselink et al. (2019) that whether the switch from negative cross-correlation to positive cross-correlation of long-wave surface elevations along the reef $\zeta_{LW}(x,t)$ and radiation stress at the forereef toe $S(x_{toe},t)$ such as that displayed by Fig. 4a–b indicates a transition from bound long wave to breakpoint forced long wave or the breakpoint forced long wave overpowering the bound long wave. The excellent balance between positive $\partial F^+/\partial x$ and R^+ obtained in this study (Fig. 6) supports the former explanation and indicates that the generation of breakpoint-forced long wave dominates over the dissipation of bound long wave in the surf zone. As reef submergence increases, the decay of bound long wave is weakened, but the growth of breakpoint-forced long wave is suppressed even more, leading to a smaller but still positive net energy transfer from short to long waves.

Note that breakpoint-forced long wave is always stronger than bound long wave over the reef with a steep forereef (Cases A–C). However, in the case of large reef submergence, this seems to violate the common conjecture that the breakpoint forcing is not effective when short waves mainly break over the horizontal reef flat (*e.g.*, Case C). An additional simulation with a larger relative submergence ($h_r/H_{SW,0} = 1.67$) also generated stronger breakpoint-forced long waves (not shown). The rationale is that the efficiency of breakpoint forcing is fundamentally related to the ratio of breakpoint excursion to long-wave length (Baldock et al., 2000; Padilla and Alsina, 2018). The outer breakpoint position moves shoreward over the forereef with increasing submergence, while the inner breakpoint is expected to be located at the reef edge where the bottom becomes horizontal because the breaker index over a horizontal bottom is solely a function of water depth (Raubenheimer et al., 1996). Therefore, the breakpoint excursion becomes smaller at larger submergence, efficiently driving breakpoint-forced long wave over the reef flat. This highlights that the wave group forcing regime is not locally controlled, and the breaking history of short waves over the forereef also influences the energy transfer direction over the reef flat. As long as the forereef is steep, the breakpoint-forced long wave prevails over the reef flat, even though the bottom slope of the reef flat is zero, consistent with the results of Masselink et al. (2019). This finding extends the work by Li et al. (2020) and Liao et al. (2021) that recognized the effects of wave spatial evolution history during shoaling on the subsequent nonlinear energy transfer between long and short waves under non-breaking conditions.

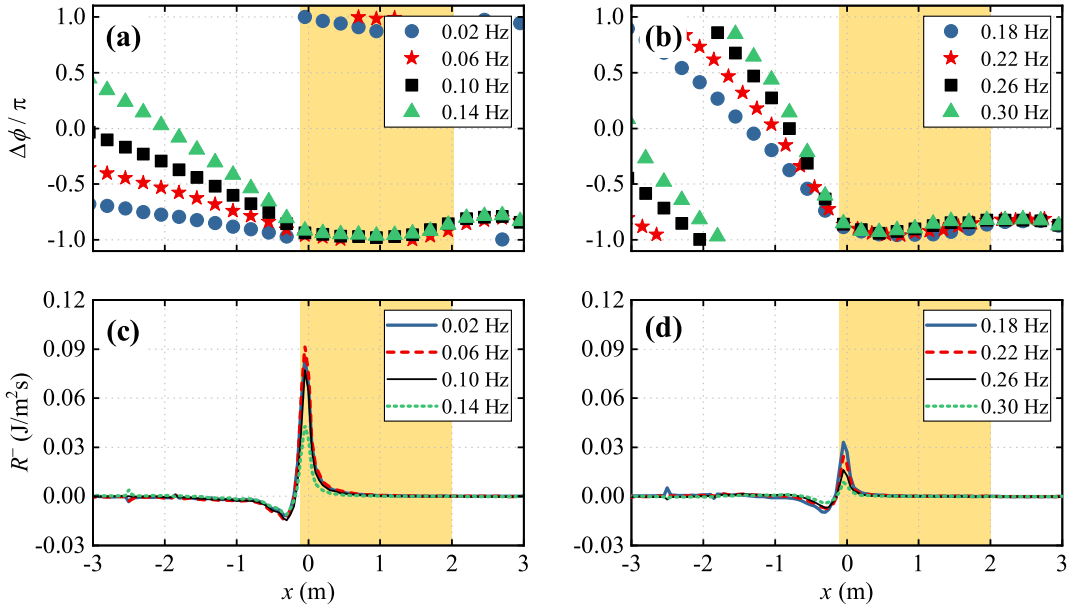

Fig. 10. (a)–(b) Phase differences and (c)–(d) energy transfer rates between outgoing long waves and the short-wave groups at each frequency component. The energy transfer rate R^- is calculated using the co-spectrum between $-U$ (Eq. (8)) and $\partial S/\partial x$. $R^- > 0$ means an energy transfer from short waves to outgoing long waves, and $R^- < 0$ suggests the opposite. Case B, $h_r = 0.045$ m and $\tan\alpha = 1/5$, where h_r is the reef submergence, and $\tan\alpha$ is the slope of the forereef. The light-yellow area indicates the surf zone.

Since the large roughness of natural coral reefs plays an important role in wave attenuation, and therefore, the energy-flux balance, additional simulations with Manning coefficient $n = 0.05$ s/m$^{1/3}$ and $0 \leq h_r/H_{SW,0} \leq 1.75$ were conducted further. It was observed that adopting the high Manning coefficient did not change the patterns of energy transfers ($R^{\pm}$) along the reef (Fig. 11a–b) but affected magnitudes of the net energy transfer from short waves to incoming long waves ($R^{+,INT} = \int_{-3}^{2} R^{+}\,dx$) (Fig. 11c). Meanwhile, the frictional dissipation ($D^{+,INT} = \int_{-3}^{2} D^{+}\,dx$) was greatly enhanced by the larger Manning coefficient ($n = 0.05$ s/m$^{1/3}$), resulting in smaller increments in incoming energy flux ($R^{+,INT} + D^{+,INT}$) and consequently smaller H_{LW}^{+} (Fig. 11c–d), compared with those with $n = 0.025$ s/m$^{1/3}$. Nevertheless, H_{LW}^{+} at $x = 2$ m still attains a peak at $h_r/H_{SW,0} = 0.3 - 0.5$ (Fig. 11d), consistent with the findings of Beetham et al. (2016) under moderate conditions and Masselink et al. (2019).

6. Conclusions

The evolution of long waves over a reef has been investigated using fully nonlinear analysis of SWASH model results. Unlike previous studies which applied a shoreline at the reef end, a wave absorbing boundary was prescribed at the reef end to minimize the influence of reef-flat resonance on the long-wave energy to focus on the long-wave evolution driven by short-wave group forcing. The long-wave velocity U was accurately calculated using the velocity profile predicted by the SWASH model and then employed to separate incoming and outgoing long waves with mass conservation to avoid the methodological error of the conventional method based on single-point velocity measurements. It was found that the incoming long-wave height increases towards the inner surf zone, and the outgoing long-wave height increases seaward in the surf zone but decreases in the forereef de-shoaling region at a rate faster than Green's law.

The fully nonlinear energy balance analysis was used to explain the cross-reef variations of long waves. It was shown that the cross-reef gradient of long-wave energy flux is mainly attributed to the nonlinear energy transfer between long and short waves which equals the work done by radiation-stress gradient on the long-wave velocity, *i.e.*, $-U\,(\partial S/\partial x)$. This proves that $-U\,(\partial S/\partial x)$ applies to both free and bound long waves since they co-exist over the reef. The incoming long waves acquire energy from short waves in shoaling and surf zones, whereas the outgoing long waves are amplified in the surf zone but weakened during de-shoaling due to the energy transfer back to short waves. This considerable net energy transfer from outgoing free long waves to incoming short-wave groups occurs just seaward of the breakpoint, where their phase differences at all frequencies remain in the same quadrant, which drives consistent energy transfers from outgoing long waves to incoming short waves at these frequencies.

The reef submergence affects the type and intensity of long waves in the surf zone from the aspects of the generation of breakpoint-forced long waves, the reduction of bound long waves, and frictional dissipation. Results indicate that the efficiency of moving-breakpoint forcing is high as long as the forereef is steep, and the amount of breakpoint-forced long wave energy depends on the thoroughness of short-wave breaking over the reef flat. As the submergence decreases, the decay of bound long wave increases, but the growth of breakpoint-forced long wave increases more, resulting in a larger net energy transfer from short to long waves and a smaller proportion of bound long waves in the incoming long waves. Large roughness of coral-reef surfaces does not change the patterns of the energy transfer but reduces the magnitude of net transferred energy. With the influences of roughness, incoming long-wave height on the reef flat first increases but then decreases with decreasing reef submergence.

The variations of wave height, energy, and nonlinear energy transfer over the reef obtained from the fully nonlinear analysis deviate significantly from those by the linear and weakly nonlinear analyses of previous studies. The present results highlight that U must incorporate contributions from the Stokes transport and the long-wave modulation of local water depth. Other existing approximation approaches lead to a significant methodological error. For example, U derived by applying low-pass filtering to single-point velocity data leads to linear analysis results that overestimate the growth of incoming long waves in the shoaling region, exhibit a drastic non-physical reduction for incoming long waves in the outer surf zone, and underestimate the incoming long waves over the reef flat. The weakly nonlinear analysis is more accurate than the linear analysis but still underestimates long waves, especially for large long-wave height to local water depth ratio. More importantly, both the linear and weakly nonlinear analyses conclude that the dissipation of bound long wave overcomes the generation of breakpoint-forced long wave in the surf zone, which contrasts with the fully nonlinear analysis findings.

CRediT authorship contribution statement

Ye Liu: Methodology, Formal analysis, Writing – original draft. **Yu Yao:** Methodology, Formal analysis. **Zhiling Liao:** Conceptualization, Methodology, Writing – review & editing. **Shaowu Li:** Supervision,

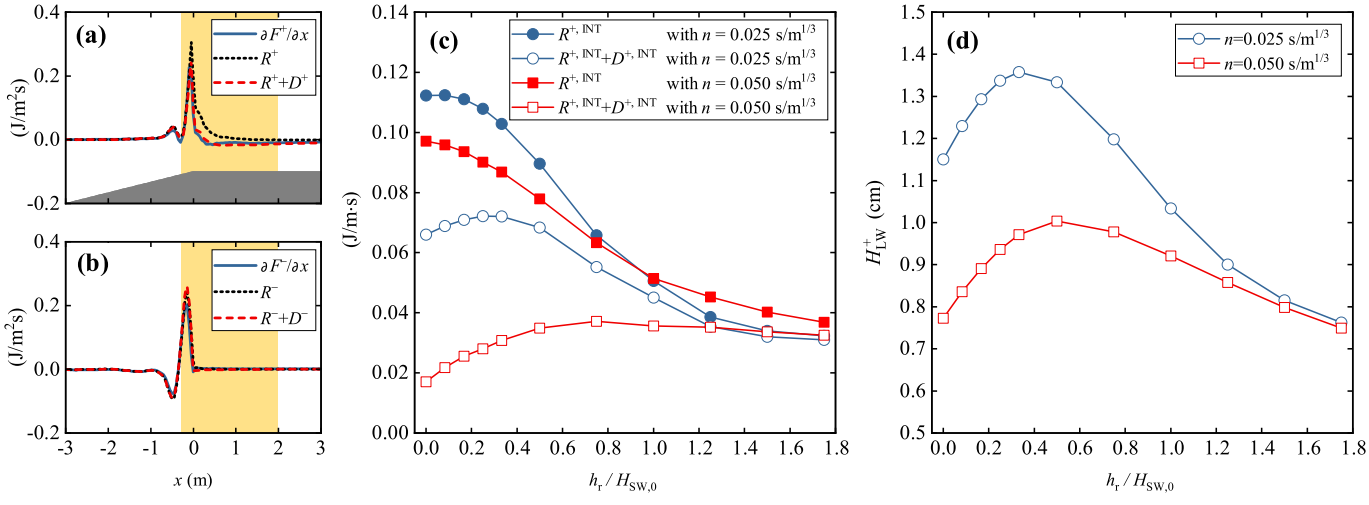

Fig. 11. Cross-reef variations of (a) incoming (+) and (b) outgoing (-) energy-flux gradient ($\partial F/\partial x$), the work done by the radiation-stress gradient (R), and the energy dissipation rate due to bottom friction (D) in an additional simulation with relative reef submergences ($h_r/H_{SW,0}$) of 0.25, forereef slope of 1/5, and Manning coefficient (n) of 0.05 s/m$^{1/3}$. Variations of (c) spatial integrals of R^{+} and D^{+} from the forereef toe ($x = -3$ m) to the end of surf zone ($x = 2$ m) and (d) height of incoming long waves at $x = 2$ m under different conditions of $h_r/H_{SW,0}$ and n.

Writing – review & editing, Funding acquisition. **Chi Zhang:** Writing – review & editing. **Qingping Zou:** Supervision, Writing – review & editing.

Declaration of competing interest

The authors declare that they have no known competing financial interests or personal relationships that could have appeared to influence the work reported in this paper.

Data availability

Data will be made available on request.

Acknowledgments

We would like to thank Prof. Tom Baldock and Prof. Robert T. Guza for discussing the release condition of bound long waves and nonlinear interaction among harmonics, respectively, Prof. Ap Van Dongeren for providing spectral analysis codes, Prof. Gerd Masselink for discussing the influence of reef submergence, and Dr. Dirk P. Rijnsdorp for helping in setting the SWASH model. This research work was supported by the National Natural Science Foundation of China (Grant No. 52201333) and the Open Foundation of Key Laboratory of Water-Sediment Sciences and Water Disaster Prevention of Hunan Province (Grant No. 2021SS03). Zhiling Liao and Qingping Zou would like to acknowledge the support by Natural Environment Research Council (NERC) of UK (Grant No. NE/V006088/1).

Appendix A. Validation of SWASH model

The experimental data of Masselink et al. (2019) were used to validate the SWASH model. Figs. A.12–A.13 suggest that the SWASH model can simulate the observed wave transformation over reefs with good accuracy.

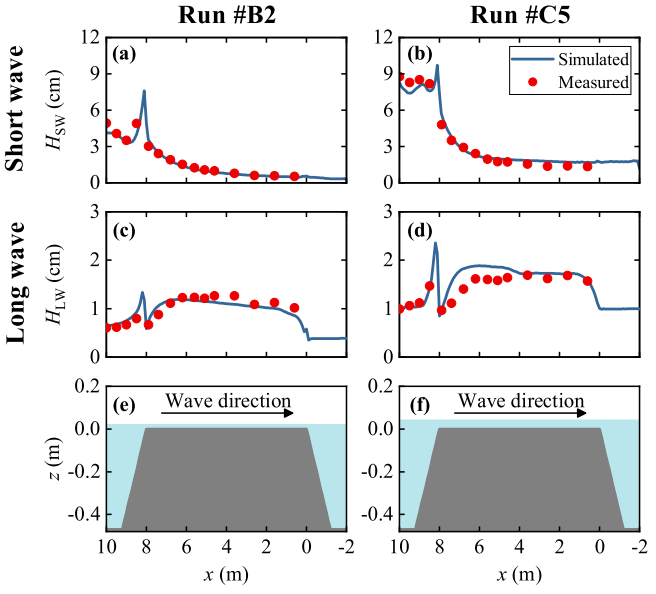

Fig. A.12. Comparisons between SWASH simulated (blue solid line) and Masselink et al. (2019) measured (red dots) (a)–(b) short-wave (H_{SW}) and (c)–(d) long-wave (H_{LW}) heights; (e)–(f) Topography of the platform reef (gray area) and the still water (blue area). Left panels, Run #B2: h_r = 0.02 m, $H_{SW,0}$ = 0.04 m, and T_p = 2.3 s; Right panels, Run #C5: h_r = 0.04 m, $H_{SW,0}$ = 0.08 m, and T_p = 1.4 s.

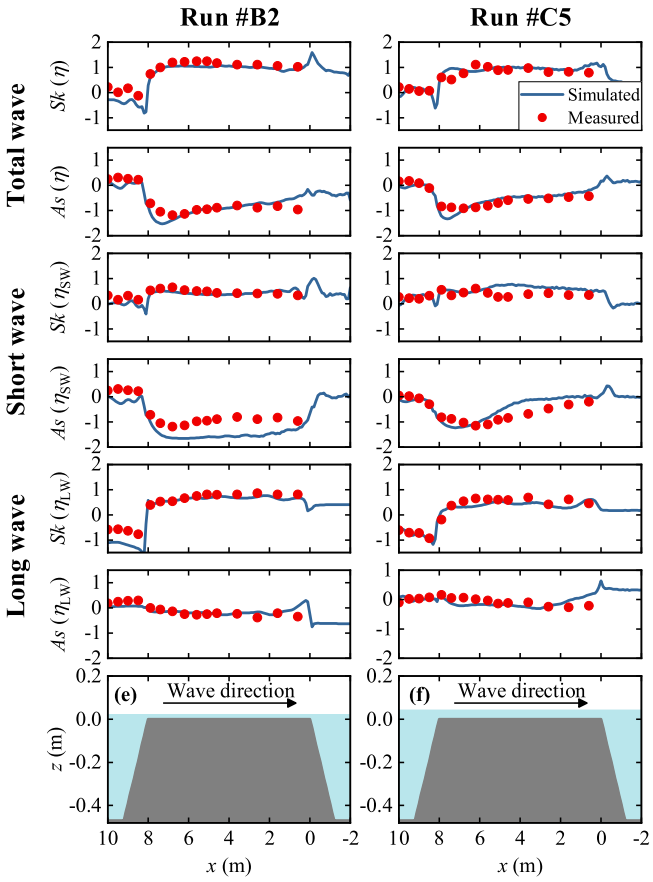

Fig. A.13. Comparisons between SWASH simulated (blue solid line) and Masselink et al. (2019) measured (red dots) skewness (Sk) and asymmetry (As) of waves across the platform reef. Bottom panels, topography of the platform reef (gray area) and the still water (blue area). Left panels, Run #B2: h_r = 0.02 m, $H_{SW,0}$ = 0.04 m, and T_p = 2.3 s; Right panels, Run #C5: h_r = 0.04 m, $H_{SW,0}$ = 0.08 m, and T_p = 1.4 s.

Appendix B. Reasonability of the adopted boundary conditions

To demonstrate the reasonability of the adopted boundary conditions, the spectrum of incoming short waves off the reef (x = −4 m, kh = 1.32) of Case B was calculated based on the method of Mansard and Funke (1980) and compared with the targeted JONSWAP spectrum in Fig. A.14a, which shows an excellent agreement. Surface elevations of total (simulated), incoming, and outgoing short waves are shown in Fig. A.14b. Since the reflection is weak, the nonlinear interaction between the incident and reflected short waves at the boundary is expected to be negligible. Incoming long-wave surface elevations were calculated using Eq. (13) and compared with the theoretical solution of Hasselmann (1962) in Fig. A.14c, which indicates that the spurious free long waves were efficiently suppressed at the inlet and the re-reflection was negligible. In addition, incoming bound long waves were skewed with deep troughs at the moments of large short waves.

Appendix C. Remainder term in separating incoming and outgoing long-wave energy fluxex

The remainder term in Eq. (17) is expressed as

$$F^{E} = \overline{U^{+}\left(h+\bar{\bar{\zeta}}+\zeta^{+}\right)\left[\frac{1}{2}\rho(U^{-})^{2}+\rho U^{+}U^{-}+\rho g\zeta^{-}\right]} + \overline{U^{-}\left(h+\bar{\bar{\zeta}}+\zeta^{-}\right)\left[\frac{1}{2}\rho(U^{+})^{2}+\rho U^{+}U^{-}+\rho g\zeta^{+}\right]} + \overline{(U^{+}\zeta^{-}+U^{-}\zeta^{+})\left[\frac{1}{2}\rho(U^{+}+U^{-})^{2}+\rho g\left(\bar{\bar{\zeta}}+\zeta^{+}+\zeta^{-}\right)\right]}.$$

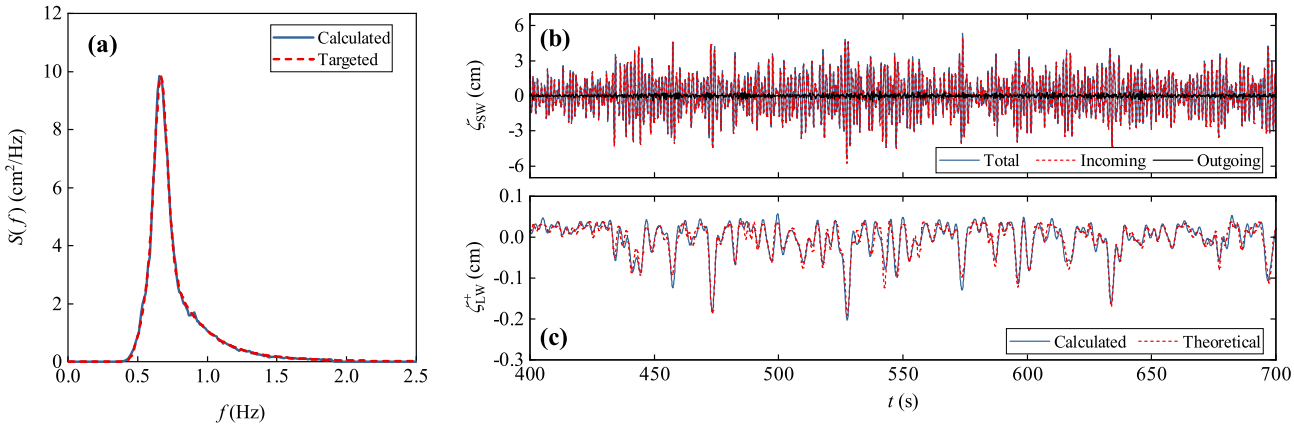

Fig. A.14. Wave information of in the off-reef region ($x = -4$ m, $kh = 1.32$) of Case B. (a) Spectrum of calculated incident short waves (blue solid line) and targeted (red dotted line) JONSWAP spectrum. (b) Water surface elevations of total (simulated, blue solid line), incoming (red dotted line), and outgoing (black solid line) short waves. (c) Calculated (blue solid line) and theoretical (red dotted line) incoming bound long waves.

References

Baldock, T.E., 2012. Dissipation of incident forced long waves in the surf zone—Implications for the concept of "bound" wave release at short wave breaking. Coastal Eng. 60, 276–285. http://dx.doi.org/10.1016/j.coastaleng.2011.11.002.

Baldock, T.E., Huntley, D.A., Bird, P.A.D., O'Hare, T., Bullock, G.N., 2000. Breakpoint generated surf beat induced by bichromatic wave groups. Coastal Eng. 39, 213–242. http://dx.doi.org/10.1016/S0378-3839(99)00061-7.

Battjes, J.A., Bakkenes, H., Janssen, T., Van Dongeren, A., 2004. Shoaling of subharmonic gravity waves. J. Geophys. Res. 109, C02009. http://dx.doi.org/10.1029/2003JC001863.

Beetham, E., Kench, P.S., O'Callaghan, J., Popinet, S., 2016. Wave transformation and shoreline water level on Funafuti Atoll, Tuvalu. J. Geophys. Res. Oceans 121, 311–326. http://dx.doi.org/10.1002/2015JC011246.

Brocchini, M., 2020. Wave-forced dynamics in the nearshore and river mouths. Earth Surf. Proc. Landf. 45 (1), 75–95. http://dx.doi.org/10.1002/esp.4699.

Buckley, M.L., Lowe, R.J., Hansen, J.E., Van Dongeren, A.R., Storlazzi, C.D., 2018. Mechanisms of wave-driven water level variability on reef-fringed coastlines. J. Geophys. Res. Oceans 123, 3811–3831. http://dx.doi.org/10.1029/2018JC013933.

Chen, H., Zou, Q., 2018. Characteristics of wave breaking and blocking by spatially varying opposing currents. J. Geophys. Res. 123 (5), 3761–3785. http://dx.doi.org/10.1029/2017JC013440.

Cheriton, O., Storlazzi, C., Rosenberger, K., 2016. Observations of wave transformation over a fringing coral reef and the importance of low-frequency waves and offshore water levels to runup, overwash, and coastal flooding. J. Geophys. Res. Oceans 121, 3121–3140. http://dx.doi.org/10.1002/2015JC011231.

Contardo, S., Symonds, G., Dufois, F., 2018. Breakpoint forcing revisited: Phase between forcing and response. J. Geophys. Res. Oceans 123, 1354–1363. http://dx.doi.org/10.1002/2017jc013138.

da Silva, R.F., Rijnsdorp, D.P., Hansen, J.E., Lowe, R., Buckley, M., Zijlema, M., 2021. An efficient method to calculate depth-integrated, phase-averaged momentum balances in non-hydrostatic models. Ocean Model. 165, 101846. http://dx.doi.org/10.1016/j.ocemod.2021.101846.

De Bakker, A.T.M., Brinkkemper, J.A., van der Steen, F., Tissier, M.F.S., G., R.B., 2016a. Cross-shore sand transport by infragravity waves as a function of beach steepness. J. Geophys. Res. Earth Surf. 121, 1786–1799. http://dx.doi.org/10.1002/2016JF003878.

De Bakker, A.T.M., Tissier, M.F.S., Ruessink, B.G., 2016b. Beach steepness effects on nonlinear infragravity-wave interactions: A numerical study. J. Geophys. Res. Oceans 121, 554–570. http://dx.doi.org/10.1002/2015JC011268.

Gao, J., Ma, X., Dong, G., Chen, H., Liu, Q., Zhang, J., 2021. Investigation on the effects of Bragg reflection on harbor oscillations. Coastal Eng. 170, 103977. http://dx.doi.org/10.1016/j.coastaleng.2021.103977.

Hasselmann, K., 1962. On the non-linear energy transfer in a gravity-wave spectrum Part 1. general theory. J. Fluid Mech. 12, 481–500. http://dx.doi.org/10.1017/s0022112062000373.

Henderson, S.M., Guza, R.T., Elgar, S., Herbers, T.H.C., Bowen, A.J., 2006. Nonlinear generation and loss of infragravity wave energy. J. Geophys. Res. 111, C12007. http://dx.doi.org/10.1029/2006jc003539.

Herbers, T.H.C., Burton, M.C., 1997. Nonlinear shoaling of directionally spread waves on a beach. J. Geophys. Res. Oceans 102, 21101–21114. http://dx.doi.org/10.1029/97jc01581.

Janssen, T., Battjes, J., van Dongeren, A., 2003. Long waves induced by short-wave groups over a sloping bottom. J. Geophys. Res. 108 (C8), 3252. http://dx.doi.org/10.1029/2002JC001515,2003.

Lara, J., Ruju, A., Losada, I., 2011. Reynolds averaged Navier-Stokes modelling of long waves induced by a transient wave group on a beach. Proc. R. Soc. Lond. Ser. A Math. Phys. Eng. Sci. 467, 1215–1242. http://dx.doi.org/10.1098/rspa.2010.0331.

Lashley, C.H., Bricker, J.D., van der Meer, J., Corrado, A., Suzuki, T., 2020. Relative magnitude of infragravity waves at coastal dikes with whallow foreshores: A prediction tool. J. Waterw. Port Coast. Ocean Eng. 146 (5), 04020034. http://dx.doi.org/10.1061/(ASCE)WW.1943-5460.0000576.

Li, S., Liao, Z., Liu, Y., Zou, Q., 2020. Evolution of infragravity waves over a shoal under nonbreaking conditions. J. Geophys. Res. Oceans 125, http://dx.doi.org/10.1029/2019JC015864, e2019JC015864.

Liao, Z., Li, S., Liu, Y., Zou, Q., 2021. An analytical spectral model for infragravity waves over topography in intermediate and shallow water under non-breaking conditions. J. Phys. Oceanogr. 51, 2749–2765. http://dx.doi.org/10.1175/JPO-D-20-0164.1.

Liao, Z., Li, S., Paniagua-Arroyave, J., Liu, Y., Zou, Q., 2022. Infragravity wave amplification by isolated topography: Field observations and semi-analytical modeling. Appl. Ocean Res. 122, 103119. http://dx.doi.org/10.1016/j.apor.2022.103119.

Liu, Y., Li, S., 2018. Variation of wave groupiness across a fringing reef. J. Waterw. Port Coast. Ocean Eng. 144, 04018022. http://dx.doi.org/10.1016/j.apor.2020.102166.

Liu, Y., Li, S., Chen, S., Hu, C., Fan, Z., Jin, R., 2020. Random wave overtopping of vertical seawalls on coral reefs. Appl. Ocean Res. 100, 102166. http://dx.doi.org/10.1016/j.apor.2020.102166.

Liu, Y., Li, S., Liao, Z., Liu, K., 2021a. Physical and numerical modeling of random wave transformation and overtopping on reef topography. Ocean Eng. 220, 108390. http://dx.doi.org/10.1016/j.oceaneng.2020.108390.

Liu, Y., Liao, Z., Fang, K., Li, S., 2021b. Uncertainty of wave runup prediction on coral reef-fringed coasts using SWASH model. Ocean Eng. 242, 110094. http://dx.doi.org/10.1016/j.oceaneng.2021.110094.

Longuet-Higgins, M.S., Stewart, R.W., 1962. Radiation stress and mass transport in gravity waves, with application to 'surf beats'. J. Fluid Mech. 13, 481–504. http://dx.doi.org/10.1017/S0022112062000877.

Lowe, R., Buckley, M., Altomare, C., Rijnsdorp, D., Yao, Y., Suzuki, T., Bricker, J., 2019. Numerical simulations of surf zone wave dynamics using "Smoothed Particle Hydrodynamics". Ocean Model. 144, 101481. http://dx.doi.org/10.1016/j.ocemod.2019.101481.

Lowe, R.J., Leon, A.S., Symonds, G., Falter, J.L., Gruber, R., 2015. The intertidal hydraulics of tide-dominated reef platforms. J. Geophys. Res. Oceans 120, 4845–4868. http://dx.doi.org/10.1002/2015jc010701.

Mansard, E., Funke, E.R., 1980. The measurement of incident and reflected spectra using a least squares method. In: 17th Int. Conf. on Coastal Eng.. ASCE, Reston, VA, pp. 154–172.

Masselink, G., Tuck, M., McCall, R., Van Dongeren, A., Ford, M., Kench, P., 2019. Physical and numerical modeling of infragravity wave generation and transformation on coral reef platforms. J. Geophys. Res. Oceans 124, 1410–1433. http://dx.doi.org/10.1029/2018JC014411.

Mei, C.C., Stiassnie, M.A., Yue, D.K.P., 2005. Theory and Applications of Ocean Surface Waves. World Scientific, Singapore.

Melito, L., Parlagreco, L., Devoti, S., Brocchini, M., 2022. Wave- and tide- Induced infragravity dynamics at an intermediate-to-dissipative microtidal beach. J. Geophys. Res. Oceans 127, http://dx.doi.org/10.1029/2021JC017980, e2021JC017980.

Melito, L., Postacchini, M., Sheremet, A., Calantoni, J., Zitti, G., Darvini, G., Penna, P., Brocchini, M., 2020. Hydrodynamics at a microtidal inlet: Analysis of propagation of the main wave components. Est. Coast. Shelf Sci. 235, 106603. http://dx.doi.org/10.1016/j.ecss.2020.106603.

Mendes, D., Pinto, J.P., Pires-Silva, A.A., Fortunato, A.B., 2018. Infragravity wave energy changes on a dissipative barred beach: A numerical study. Coastal Eng. 140, 136–146. http://dx.doi.org/10.1016/j.coastaleng.2018.07.005.

Moura, T., Baldock, T.E., 2019. The influence of free long wave generation on the shoaling of forced infragravity waves. J. Mar. Sci. Eng. 7, http://dx.doi.org/10.3390/jmse7090305.

Padilla, E.M., Alsina, J.M., 2018. Long wave generation induced by differences in the wave-group structure. J. Geophys. Res. Oceans 123, 8921–8940. http://dx.doi.org/10.1029/2018JC014213.

Péquignet, A.-C.N., Becker, J.M., Merrifield, M.A., 2014. Energy transfer between wind waves and low-frequency oscillations on a fringing reef, Ipan, Guam. J. Geophys. Res. Oceans 119, 6709–6724. http://dx.doi.org/10.1002/2014JC010179.

Phillips, O.M., 1977. The Dynamics of the Upper Ocean. Cambridge University Press, Cambridge.

Pomeroy, A., Lowe, R., Symonds, G., Van Dongeren, A., Moore, C., 2012. The dynamics of infragravity wave transformation over a fringing reef. J. Geophys. Res. 117, C11022. http://dx.doi.org/10.1029/2012JC008310.

Pomeroy, A.W.M., Lowe, R.J., Van Dongeren, A., Ghisalberti, M., Bodde, W., Roelvink, D., 2015. Spectral wave-driven sediment transport across a fringing reef. Coastal Eng. 98, 78–94. http://dx.doi.org/10.1016/j.coastaleng.2015.01.005.

Quataert, E., Storlazzi, C.D., Van Rooijen, A., Cheriton, O.M., Van Dongeren, A., 2015. The influence of coral reefs and climate change on wave-driven flooding of tropical coastlines. Geophys. Res. Lett. 42, 6407–6415. http://dx.doi.org/10.1002/2015GL064861.

Raubenheimer, B., Guza, R.T., Elgar, S., 1996. Wave transformation across the inner surf zone. J. Geophys. Res. 101, 25589–25597. http://dx.doi.org/10.1029/96JC02433.

Rijnsdorp, D.P., Ruessink, G., Zijlema, M., 2015. Infragravity-wave dynamics in a barred coastal region, a numerical study. J. Geophys. Res. Oceans 120, 4068–4089. http://dx.doi.org/10.1002/2014JC010450.

Rijnsdorp, D.P., Smit, P.B., Guza, R., 2022. A nonlinear, non-dispersive energy balance for surfzone waves: infragravity wave dynamics on a sloping beach. J. Fluid Mech. 944, A45. http://dx.doi.org/10.1017/jfm.2022.512.

Rijnsdorp, D.P., Smit, P.B., Zijlema, M., 2014. Non-hydrostatic modelling of infragravity waves under laboratory conditions. Coastal Eng. 85, 30–42. http://dx.doi.org/10.1016/j.coastaleng.2013.11.011.

Risandi, J., Rijnsdorp, D.P., Hansen, J.E., Lowe, R.J., 2020. Hydrodynamic modeling of a reef-fringed pocket beach using a phase-resolved non-hydrostatic model. J. Mar. Sci. Eng. 8, http://dx.doi.org/10.3390/jmse8110877.

Roeber, V., Bricker, J., 2015. Destructive tsunami-like wave generated by surf beat over a coral reef during Typhoon Haiyan. Nature Commun. 6, 7854. http://dx.doi.org/10.1038/ncomms8854.

Ruessink, B.G., van den Berg, T.J.J., van Rijn, L.C., 2009. Modeling sediment transport beneath skewed asymmetric waves above a plane bed. J. Geophys. Res. Oceans 114, C11021. http://dx.doi.org/10.1029/2009JC005416.

Ruju, A., Lara, J.L., Losada, I.J., 2012. Radiation stress and low-frequency energy balance within the surf zone: A numerical approach. Coastal Eng. 68, 44–55. http://dx.doi.org/10.1016/j.coastaleng.2012.05.003.

Schäffer, H.A., 1993. Infragravity waves induced by short-wave groups. J. Fluid Mech. 247, 551–588. http://dx.doi.org/10.1017/S0022112093000564.

Sheremet, A., Guza, R.T., Elgar, S., Herbers, T.H.C., 2002. Observations of nearshore infragravity waves: Seaward and shoreward propagating components. J. Geophys. Res. 107, 3095. http://dx.doi.org/10.1029/2001JC000970.

Svendsen, I.A., 1984. Wave heights and set-up in a surf zone. Coastal Eng. 8, 303–329. http://dx.doi.org/10.1016/0378-3839(84)90028-0.

Symonds, G., Huntley, D.A., Bowen, A.J., 1982. Two-dimensional surf beat: Long wave generation by a time-varying breakpoint. J. Geophys. Res. 81, 492–498. http://dx.doi.org/10.1029/JC087iC01p00492.

Thotagamuwage, D.T., Pattiaratchi, C.B., 2014. Influence of offshore topography on infragravity period oscillations in two rocks marina, western australia. Coastal Eng. 91, 220–230. http://dx.doi.org/10.1016/j.coastaleng.2014.05.011.

Torres-Freyermuth, A., Marino-Tapia, I., Coronado, C., Salles, P., Medellin, G., Pedrozo-Acuna, A., Silva, R., Candela, J., Iglesias-Prieto, R., 2012. Wave-induced extreme water levels in the Puerto Morelos fringing reef lagoon. Nat. Hazard. Earth Sys. 12, 3765–3773. http://dx.doi.org/10.5194/nhess-12-3765-2012.

Van Dongeren, A., Battjes, J., Janssen, T., Van Noorloos, J., Steenhauer, K., Steenbergen, G., Reniers, A., 2007. Shoaling and shoreline dissipation of low-frequency waves. J. Geophys. Res. 112, C02011. http://dx.doi.org/10.1029/2006JC003701.

Van Dongeren, A., Lowe, R., Pomeroy, A., Trang, D.M., Roelvink, D., Symonds, G., Ranasinghe, R., 2013. Numerical modeling of low-frequency wave dynamics over a fringing coral reef. Coastal Eng. 73, 178–190. http://dx.doi.org/10.1016/j.coastaleng.2012.11.004.

Van Dongeren, A., Svendsen, I.A., 1997. Quasi 3-D modeling of nearshore hydrodynamics. Report, Center for Applied Coastal Research, University of Delaware.

Wang, Z., Zou, Q., Reeve, D.E., 2009. Simulation of spilling breaking waves using a two phase flow CFD model. Comput. Fluids 38 (10), 1995–2005. http://dx.doi.org/10.1016/j.compfluid.2009.06.006.

Yao, Y., Becker, J.M., Ford, M.R., Merrifield, M.A., 2016. Modeling wave processes over fringing reefs with an excavation pit. Coastal Eng. 109, 9–19. http://dx.doi.org/10.1016/j.coastaleng.2015.11.009.

Yao, Y., Huang, Z., Monismith, S.G., Lo, E.Y.M., 2013. Characteristics of monochromatic waves breaking over fringing reefs. J. Coastal Res. 29, 94–104. http://dx.doi.org/10.2112/JCOASTRES-D-12-00021.1.

Yao, Y., Jia, M., Jiang, C., Zhang, Q., Tang, Z., 2020. Laboratory study of wave processes over fringing reefs with a reef-flat excavation pit. Coastal Eng. 158, 103700. http://dx.doi.org/10.1016/j.coastaleng.2020.103700.

Zheng, J., Yao, Y., Chen, S.G., Chen, S.B., Zhang, Q., 2020. Laboratory study on wave-induced setup and wave-driven current in a 2DH reef-lagoon-channel system. Coastal Eng. 162, 103772. http://dx.doi.org/10.1016/j.coastaleng.2020.103772.

Zhu, G., Ren, B., Dong, P., Wang, G., Chen, W., 2021. Experimental investigation on the infragravity wave on different reef systems under irregular wave action. Ocean Eng. 226, 108851. http://dx.doi.org/10.1016/j.oceaneng.2021.108851.

Zijlema, M., Stelling, G., Smit, P., 2011. SWASH: An operational public domain code for simulating wave fields and rapidly varied flows in coastal waters. Coastal Eng. 58, http://dx.doi.org/10.1016/j.coastaleng.2011.05.015.

Zou, Q., 2011. Generation, transformation, and scattering of long waves induced by a short-wave group over finite topography. J. Phys. Oceanogr. 41, 1842–1859. http://dx.doi.org/10.1175/2011JPO4511.1.

Zou, Q., Bowen, A.J., Hay, A.E., 2006. Vertical distribution of wave shear stress in variable water depth: Theory and field observations. J. Geophys. Res. Oceans 111 (C9), C09032. http://dx.doi.org/10.1029/2005JC003300.

Zou, Q., Hay, A.E., Bowen, A.J., 2003. Vertical structure of surface gravity waves propagating over a sloping seabed: Theory and field measurements. J. Geophys. Res. Oceans 108 (C8), 3265. http://dx.doi.org/10.1029/2002JC001432.

Zou, Q., Peng, Z., 2011. Evolution of wave shape over a low-crested structure. Coastal Eng. 58, 478–488. http://dx.doi.org/10.1016/j.coastaleng.2011.01.001.